Since January 2020 Elsevier has created a COVID-19 resource centre with free information in English and Mandarin on the novel coronavirus COVID-19. The COVID-19 resource centre is hosted on Elsevier Connect, the company's public news and information website.

Article

Immunity

Uncoupling of macrophage inflammation from self-renewal modulates host recovery from respiratory viral infection

Graphical abstract

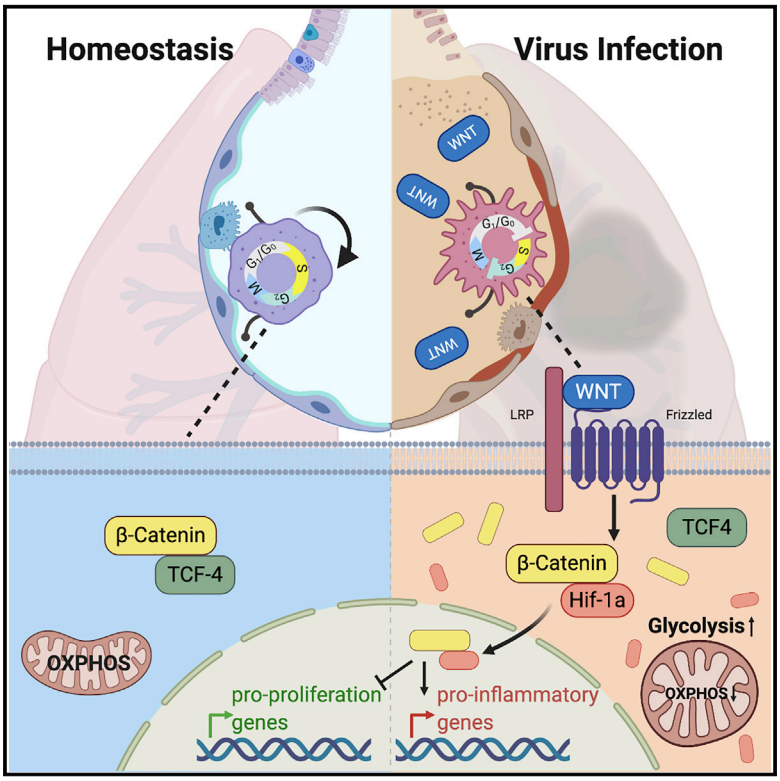

Highlights

- Wnt-β-catenin signaling modulates AM inflammation and self-renewal through HIF-1α
- AM β-catenin and HIF-1α signaling promotes host diseases and inhibits lung recovery
- HIF-1α activity separates AM inflammatory activity from proliferative potential *in vivo*
- β-Catenin and HIF-1α signaling may contribute to severe disease development in COVID-19

Authors

Bibo Zhu, Yue Wu, Su Huang, ..., Xiaobo Zhou, Ananda W. Goldrath, Jie Sun

Correspondence

sun.jie@mayo.edu

In brief

Zhu et al. examine the relationship between proliferative and inflammatory properties of tissue macrophages by defining the impact of the Wnt-β-catenin pathway, a regulator of self-renewal, in alveolar macrophages (AMs). Their findings reveal a β-catenin-HIF-1α signaling axis that promotes inflammatory AMs at the expense of proliferation. This axis is conserved in human AMs, with implications for the treatment of severe respiratory diseases.

Zhu et al., 2021, Immunity *54*, 1200–1218
June 8, 2021
https://doi.org/10.1016/j.immuni.2021.04.001

CellPress

CellPress
OPEN ACCESS

Immunity

Article

Uncoupling of macrophage inflammation from self-renewal modulates host recovery from respiratory viral infection

Bibo Zhu,[1,2] Yue Wu,[1,2] Su Huang,[1,2] Ruixuan Zhang,[1,2] Young Min Son,[1,2] Chaofan Li,[1,2] In Su Cheon,[1,2] Xiaochen Gao,[1,2] Min Wang,[1,2] Yao Chen,[3,4] Xian Zhou,[2,5] Quynh Nguyen,[6] Anthony T. Phan,[6] Supriya Behl,[7] M. Mark Taketo,[8] Matthias Mack,[9] Virginia S. Shapiro,[2] Hu Zeng,[2,5] Hideki Ebihara,[10] John J. Mullon,[1] Eric S. Edell,[1] Janani S. Reisenauer,[1] Nadir Demirel,[7] Ryan M. Kern,[1] Rana Chakraborty,[7] Weiguo Cui,[3,4] Mark H. Kaplan,[11] Xiaobo Zhou,[12] Ananda W. Goldrath,[6] and Jie Sun[1,2,13,*]

[1]Division of Pulmonary and Critical Care Medicine, Department of Medicine, Mayo Clinic College of Medicine and Science, Rochester, MN 55905, USA
[2]Department of Immunology, Mayo Clinic College of Medicine and Science, Rochester, MN 55905, USA
[3]Versiti Blood Research Institute, Milwaukee, WI 53226, USA
[4]Department of Microbiology and Immunology, Medical College of Wisconsin, Wauwatosa, WI 53226, USA
[5]Division of Rheumatology, Department of Medicine, Mayo Clinic College of Medicine and Science, Rochester, MN 55905, USA
[6]Division of Biological Sciences, Section of Molecular Biology, University of California, San Diego, La Jolla, CA 92093, USA
[7]Department of Pediatric and Adolescent Medicine, Mayo Clinic, Rochester, MN 55905, USA
[8]Division of Experimental Therapeutics, Graduate School of Medicine, Kyoto University, Kyoto, Japan
[9]Department of Nephrology, University Hospital Regensburg, 93053 Regensburg, Germany
[10]Department of Molecular Medicine, Mayo Clinic College of Medicine and Science, Rochester, MN 55905, USA
[11]Department of Microbiology and Immunology, Indiana University School of Medicine, Indianapolis, IN 46202, USA
[12]Channing Division of Network Medicine, Department of Medicine, Brigham and Women's Hospital, Boston, MA 02115, USA
[13]Lead contact
*Correspondence: sun.jie@mayo.edu
https://doi.org/10.1016/j.immuni.2021.04.001

SUMMARY

Tissue macrophages self-renew during homeostasis and produce inflammatory mediators upon microbial infection. We examined the relationship between proliferative and inflammatory properties of tissue macrophages by defining the impact of the Wnt/β-catenin pathway, a central regulator of self-renewal, in alveolar macrophages (AMs) . Activation of β-catenin by Wnt ligand inhibited AM proliferation and stemness, but promoted inflammatory activity. In a murine influenza viral pneumonia model, β-catenin-mediated AM inflammatory activity promoted acute host morbidity; in contrast, AM proliferation enabled repopulation of reparative AMs and tissue recovery following viral clearance. Mechanistically, Wnt treatment promoted β-catenin-HIF-1α interaction and glycolysis-dependent inflammation while suppressing mitochondrial metabolism and thereby, AM proliferation. Differential HIF-1α activities distinguished proliferative and inflammatory AMs *in vivo*. This β-catenin-HIF-1α axis was conserved in human AMs and enhanced HIF-1α expression associated with macrophage inflammation in COVID-19 patients. Thus, inflammatory and reparative activities of lung macrophages are regulated by β-catenin-HIF-1α signaling, with implications for the treatment of severe respiratory diseases.

INTRODUCTION

Respiratory viruses, including influenza A virus (IAV) and severe acute respiratory syndrome coronavirus 2 (SARS-CoV-2), can cause severe host morbidity and mortality, which pose substantial threats to public health (Channappanavar and Perlman, 2017; Short et al., 2014; Zhang and Liu, 2020). A rapid and well-controlled innate immune response is the first line of defense against respiratory viral infections, but sustained and uncontrolled inflammatory responses can lead to tissue damage and severe disease (Channappanavar et al., 2016; Iwasaki and Pillai, 2014; Short et al., 2014). Therefore, better understanding the mechanisms regulating the immune-mediated protection versus immune-driven tissue damage is urgently needed for developing effective host-directive therapeutics against severe viral pneumonia.

Tissue-resident alveolar macrophages (AMs) are essential for the protection against respiratory viral infections through the production of anti-viral cytokines, phagocytosis of virus and infected cells and/or their wound-healing function to repair damaged lungs (Kumagai et al., 2007; Newton et al., 2016; Schneider et al., 2014). However, AMs can also prime and contribute to inappropriate inflammation via the recruitment of inflammatory immune cells and/or their direct release of various

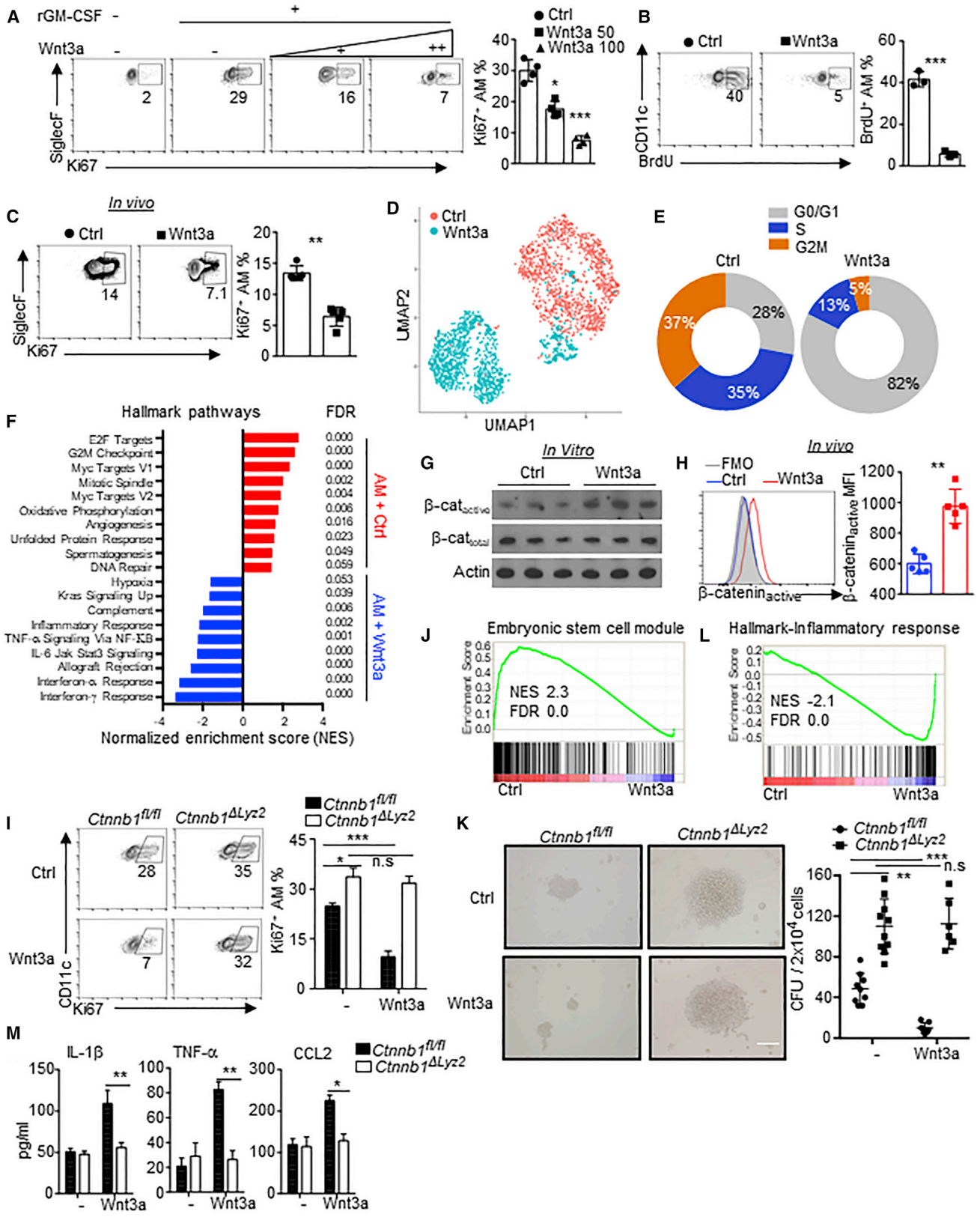

(legend on next page)

inflammatory mediators following infection (Gwyer Findlay and Hussell, 2012; Huang et al., 2019). AMs are able to maintain themselves through stem-like proliferation and self-renewal *in vivo* (Soucie et al., 2016). The mechanisms underlying the distinct, context-dependent functions of AMs are not well defined.

The canonical Wnt/β-catenin signaling pathway is an important regulator of cell growth and proliferation during tissue development and in homeostasis (Logan and Nusse, 2004). The core factor β-catenin is phosphorylated and degraded without Wnt ligand engagement. Binding of Wnt ligands to receptors inhibits β-catenin degradation, thereby activating the transcription of β-catenin target genes through the interaction of β-catenin with T cell factor (TCF)/lymphoid enhancer-binding factor (LEF) transcription factors in the nucleus (Clevers and Nusse, 2012). Wnt/β-catenin signaling is a major driver of the self-renewal of hematopoietic and tissue stem cells, and if aberrantly activated, it promotes the development of cancer (Morris and Huang, 2016; Reya et al., 2003). However, less is understood about how Wnt/β-catenin signaling affect immune cell function under disease or viral infection. Studies demonstrate that context-specific activities of Wnt/β-catenin signaling may have opposite effects in different immune cell types. For instance, activation of Wnt/β-catenin signaling in intestinal dendritic cells (DCs) shifts the balance of the production of pro- and anti-inflammatory mediators, promoting tolerance induction in the gut (Manicassamy et al., 2010; Manoharan et al., 2014). Conversely, the secretion of Wnt ligands in p53-deficient cancer cells stimulates tumor-associated macrophages to produce interleukin-1β (IL-1β), thus driving systemic inflammation (Wellenstein et al., 2019). However, the effects of Wnt/β-catenin pathway on macrophage self-renewal and function under physiological and pathological conditions are currently unknown.

Here, we examined the roles of Wnt/β-catenin signaling in regulating proliferative and inflammatory fate decisions of lung resident macrophages *in vivo* upon respiratory viral infection. We found that activation of the Wnt/β-catenin signaling suppressed proliferation and self-renewal of AMs and simultaneously promoted AM production of proinflammatory mediators. Wnt signaling in AMs led to the assembly of a "nonconventional" β-catenin-HIF-1α complex, thereby promoting glycolysis-dependent inflammation while suppressing mitochondrial metabolism-dependent proliferation of AMs *in vitro* and *in vivo* following viral infection. Using a HIF-1α activity reporter mouse strain, we demonstrated that AMs with high HIF-1α activity were inflammatory and had limited proliferative capacity, while AMs with low HIF-1α activity were highly proliferative and expressed genes associated with tissue repair *in vivo* during IAV infection. In accordance, there was a transition from inflammatory AMs to wound-healing AMs during the course of infection, and the reparative AMs repopulated by proliferation were needed for optimal lung recovery following viral clearance. Further, Wnt-β-catenin-HIF-1α signaling was conserved in human AMs, and HIF-1α signaling likely promoted macrophage inflammatory activity but inhibited their self-renewal following IAV and SARS-CoV-2 infection. Our results have not only uncovered the mechanisms modulating tissue macrophage fate choices between progeny production and inflammatory effector activity *in vivo* but also reveal a key pathway that can be targeted for dampening host hyperinflammation and/or promoting fast tissue recovery during severe respiratory viral infection.

RESULTS

Wnt/β-catenin signaling suppresses AM self-renewal and promotes inflammation

AMs proliferate and self-renew autonomously, like stem cells (Hashimoto et al., 2013; Sieweke and Allen, 2013; Soucie et al., 2016). We tested the ability of Wnt ligand (Wnt3a) treatment on AMs isolated from the bronchoalveolar lavage (BAL) of wild-type (WT) mice to proliferate in the presence of granulocyte-macrophage colony-stimulating factor (GM-CSF). Wnt3a exerted a dose-dependent suppression on AM proliferation, but not cell death (Figures 1A, 1B, and S1A). The inhibitory effect of Wnt3a on AM proliferation was further confirmed with AMs from cyclin B1-GFP transgenic mice, in which GFP expression indicates S-G2-M proliferating stages (Klochendler et al., 2012) (Figure S1B). As a result, Wnt3a inhibited AM expansion (Soucie et al., 2016) (Figure S1C). Notably, Wnt3a treatment increased B16 cancer cell proliferation (Figure S1D). Additionally, intranasal inoculation of recombinant Wnt3a resulted in decreased AM Ki67 expression *in vivo* (Figures 1C).

We next performed single-cell RNA sequencing (scRNA-seq) analysis in control or Wnt3a-treated AMs. Dimensionality reduction analysis of combined control or Wnt3a-treated AMs revealed eight clusters, and control or Wnt3a-treated AMs were almost mutually exclusive, as visualized in a uniform manifold approximation and projection (UMAP) plot (Figures 1D and S1E). Cell-cycle analysis indicated that Wnt3a-treated AMs halted cell-cycle progression (Figures 1E, S1F, and S1G). Gene

Figure 1. Regulation of AM self-renewal and inflammation by Wnt/β-catenin signaling

(A) Percentage of $Ki67^+$ AMs following *in vitro* culture with indicated conditions (n = 4).

(B) Percentage of $BrdU^+$ AMs with or without Wnt3a treatment (n = 3) *in vitro*.

(C) Percentage of $Ki67^+$ AMs with or without Wnt3a treatment (n = 5) *in vivo*.

(D–F) scRNA-seq of WT AMs with or without Wnt3a treatment. (D) UMAP plot. (E) Percentage of G0/1, S, and G2M phase based on cell-cycle gene expression. (F) Normalized enrichment scores of hallmark gene sets.

(G) Active or total β-catenin levels in control or Wnt3a-treated AMs *in vitro* (n = 3).

(H) Active β-catenin levels in AMs with or without Wnt3a treatment *in vivo* (n = 5).

(I) Percentage of $Ki67^+$ AMs with indicated genotypes and treatment *in vitro* (n = 3).

(J) GSEA of core embryonic stem cell (ESC) modules (MSigDB M7079).

(K) CFUs of $Ctnnb1^{fl/fl}$ or $Ctnnb1^{\Delta Lyz2}$ AMs with or without Wnt3a treatment (n = 6–10). Scale bars, 200 μm.

(L) GSEA of inflammatory response gene set.

(M) IL-1β, TNF-α, or CCL2 levels in the supernatants of AMs with indicated genotypes and treatment (n = 3).

Data are the mean ± SEM and representative of two or three experiments (except D–F, J, and L). *, $p < 0.05$; **, $p < 0.01$; ***, $p < 0.001$. See also Figure S1.

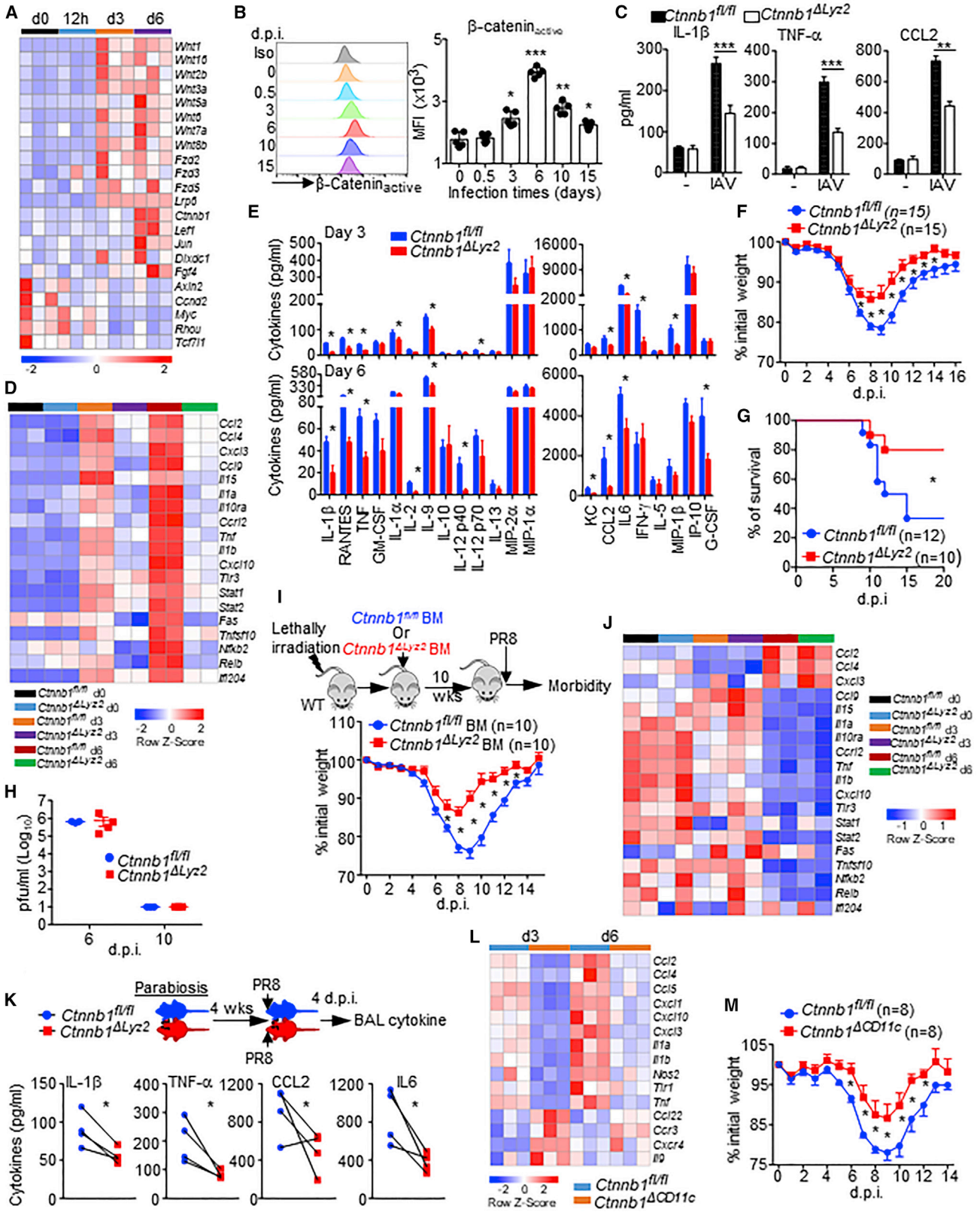

(legend on next page)

set enrichment analysis (GSEA) further revealed that gene sets that regulate cell-cycle progression were enriched in control AMs (Figures 1F and S1H). Wnt3a treatment promoted non-phosphorylated β-catenin (active β-catenin) expression *in vitro* and *in vivo*, as determined by western blot or flow cytometry (Figures 1G, 1H, and S1I), and the suppressive effects of Wnt3a on AM proliferation were dependent on β-catenin (Figures 1I). As such, Wnt3a treatment resulted in a competitive disadvantage of WT AMs compared to β-catenin-deficient AMs (Figure S1J). Further, constitutive activation of β-catenin due to the genetic deletion of *Ctnnb1* exon3 (Figure S1K) (Harada et al., 1999) led to decreased cell proliferation (Figure S1L).

An embryonic stem cell (ESC)-specific gene module is linked to macrophage stemness (Soucie et al., 2016; Wong et al., 2008). GSEA of scRNA-seq data revealed a significant reduction of ESC genes in Wnt3a-treated AMs (Figure 1J), suggesting that Wnt signaling may suppress AM stemness. Indeed, the colony-forming ability (shown as colony-forming units [CFUs]) of AMs increased in β-catenin-deficient AMs compared to WT AMs (Soucie et al., 2016) (Figure 1K). Further, Wnt3a treatment led to a reduction of colony size and numbers in WT AMs, but not in β-catenin-deficient AMs (Figure 1K). Notably, an inflammatory response gene set was enriched in Wnt3a-treated AMs (Figures 1F, 1L, and S1M), and Wnt3a treatment caused increased production of IL-1β, tumor necrosis factor alpha (TNF-α), and CCL2 in WT, but not β-catenin-deficient, AMs (Figures 1M). Thus, Wnt signaling through β-catenin promotes inflammatory activities of AMs and simultaneously suppresses AM proliferation and self-renewal capabilities.

β-Catenin deficiency in tissue-resident AMs decreases excessive pulmonary inflammation and host morbidity during IAV infection

We next sought to determine whether β-catenin modulates AM inflammation in response to pathogen infection. IAV infection upregulated a number of Wnt ligand expression in AMs from 12 h post-infection, while upregulation of active β-catenin protein occurred at ~24 h post-infection (Figures S2A–S2C) *in vitro*. *In vivo*, IAV infection induced expression of a number of Wnt ligands and target genes in AMs or in the whole lung tissue at ~3 and 6 days post-infection (d.p.i.), which were accompanied by increased active β-catenin levels in AMs, particularly at 6 d.p.i. (Figures 2A, 2B, S2C, and S2D). We then infected WT or β-catenin-deficient AMs with IAV *in vitro* and found that IL-1β, TNF-α, and CCL2 production was upregulated in AMs in a β-catenin-dependent manner (Figures 2C and S2E). We also performed NanoString analysis on 560 immune-related genes in AMs sorted from the lungs before (0) and at 3 or 6 d.p.i. (Figure S2F). β-Catenin deficiency led to diminished expression of a number of inflammatory-associated genes (such as *Ccl2*, *Tnf*, *Il1b*, *Cxcl10*, and *Nfkb2*) in AMs, particularly at 6 d.p.i. (Figure 2D), suggesting that the loss of β-catenin decreased AM inflammatory responses following IAV infection.

AMs are among the first responders sensing IAV infection (Londrigan et al., 2015; Tate et al., 2010). As such, inflammatory mediators produced by AMs could initiate and/or amplify subsequent lung inflammation by recruiting or activating other inflammatory cells such as monocytes and neutrophils through the production of chemokines, including CCL2 and IP-10 (Huang et al., 2019; Rubins, 2003). Therefore, we examined whether myeloid β-catenin deficiency would decrease overall lung inflammation during IAV infection. Myeloid β-catenin deficiency diminished airway inflammation at 3 or 6 d.p.i. (Figure 2E). In accordance with diminished production of various chemokines, myeloid β-catenin-deficient mice exhibited decreased accumulation of inflammatory monocytes (Ly6c^{+}) and neutrophils (Figure S2G), which has been reported to contribute to pulmonary immune pathology following IAV infection (Channappanavar et al., 2016; Newton et al., 2016; Zhu et al., 2019). Therefore, the difference in the cytokine levels in the BAL could be due to the decreased AM production of inflammatory cytokines per se and/or caused by diminished numbers of inflammatory monocytes and neutrophils present in the myeloid β-catenin-deficient mice compared to those of WT mice. Consequently, *Ctnnb1*$^{\Delta Lyz2}$ mice had diminished host morbidity and mortality and enhanced recovery of body temperature but similar kinetics of viral clearance compared to *Ctnnb1*$^{fl/fl}$ mice (Figures 2F–2H and S2H). Conversely, *Ctnnb1*$_{exon3}$$^{\Delta Lyz2}$ mice exhibited worsened weight loss following IAV infection (Figure S2I).

Lyz2-Cre activities have been detected in multiple cell types including macrophages, neutrophils, monocytes, and type II alveolar epithelial (ATII) cells (Cardani et al., 2017; Desai et al., 2014; Zhu et al., 2019). To rule out the potential contribution of β-catenin expression in ATII cells in regulating IAV pathogenesis, we generated bone marrow (BM) chimeric mice in which BM cells from either *Ctnnb1*$^{fl/fl}$ or *Ctnnb1*$^{\Delta Lyz2}$ mice were transferred into lethally irradiated WT mice (Figure 2I). Mice receiving BM cells from *Ctnnb1*$^{\Delta Lyz2}$ mice showed diminished host morbidity (Figure 2I). Furthermore, we have utilized a mouse model (*Ctnnb1*$^{\Delta Spc\text{-}cre\ ERT2}$) in which β-catenin expression in ATII cells

Figure 2. Loss of β-catenin decreases AM inflammation and host morbidity during IAV infection

(A) Wnt signaling pathway gene levels in sorted AMs by PCR array (n = 3).
(B) Active β-catenin levels in WT AMs at indicated d.p.i. (n = 5 mice per group).
(C) IL-1β, TNF-α, and CCL2 secretion in *Ctnnb1*$^{fl/fl}$ or *Ctnnb1*$^{\Delta Lyz2}$ AMs (n = 4) with or without IAV infection *in vitro*.
(D) NanoString analysis on inflammatory genes of AMs sorted from IAV-infected *Ctnnb1*$^{fl/fl}$ or *Ctnnb1*$^{\Delta Lyz2}$ mice at indicated d.p.i.
(E–H) *Ctnnb1*$^{fl/fl}$ or *Ctnnb1*$^{\Delta Lyz2}$ mice were infected with IAV. (E) BAL cytokine levels at 3 or 6 d.p.i. (n = 4–6). Host morbidity (F) and mortality (G) were monitored. (H) BAL viral titers at 6 or 10 d.p.i. (n = 3–4).
(I) BM chimera construction and host morbidity following IAV infection.
(J) NanoString analysis on inflammatory genes of monocytes sorted from lungs of IAV-infected *Ctnnb1*$^{fl/fl}$ or *Ctnnb1*$^{\Delta Lyz2}$ mice at indicated d.p.i.
(K) BAL cytokines of IAV-infected parabiotic mice.
(L) Inflammatory gene expression in AMs sorted from IAV-infected *Ctnnb1*$^{fl/fl}$ or *Ctnnb1*$^{\Delta CD11c}$ mice at 3 or 6 d.p.i. by PCR array.
(M) Host morbidity of *Ctnnb1*$^{fl/fl}$ or *Ctnnb1*$^{\Delta CD11c}$ following IAV infection.
Representative or pooled data (F, G, I, and M) from at least two independent experiments (except A, D, J, and L). Data are the mean ± SEM. *, $p < 0.05$; **, $p < 0.01$; ***, $p < 0.001$. See also Figures S2 and S3.

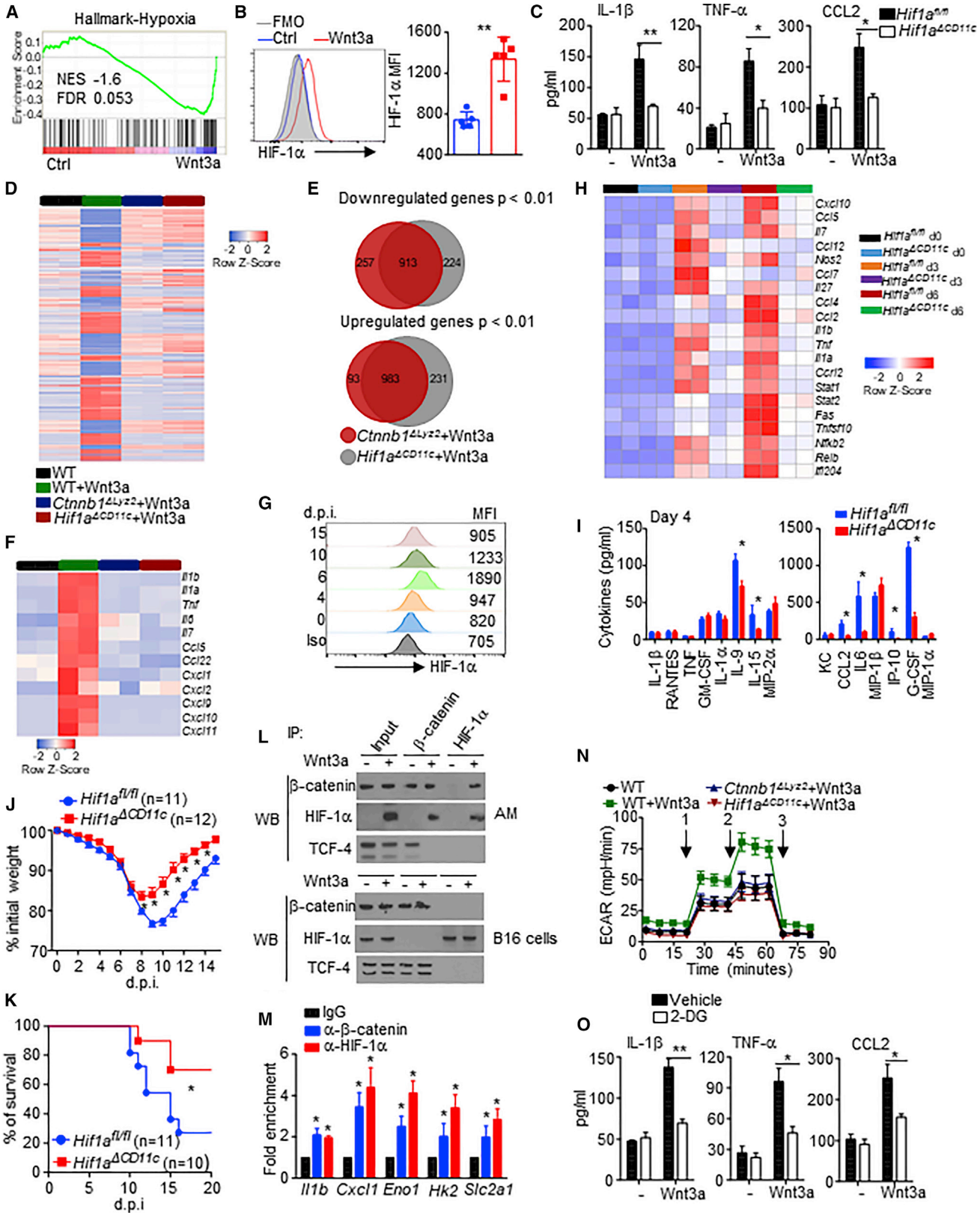

(legend on next page)

can be specifically ablated through the administration of tamoxifen. Following injection of tamoxifen, surfactant protein C (SPC)-cre activity was mainly observed in ATII cells of *Ctnnb1*$^{\Delta Spc\text{-}cre\ ERT2}$, but not *Ctnnb1*$^{fl/fl}$ mice (Figure S2J) (Chapman et al., 2011). Notably, *Ctnnb1*$^{\Delta Spc\text{-}cre\ ERT2}$ mice had similar weight loss compared to the control mice upon IAV infection (Figure S2K). These data suggest that the protective effects observed in *Ctnnb1*$^{\Delta Lyz2}$ mice following IAV infection are largely independent of β-catenin absence in ATII cells.

Ctnnb1 gene was highly expressed in AMs compared to monocytes and interstitial macrophages (Figure S2M). Consistently, monocytes isolated from WT or myeloid β-catenin deficient mice exhibited a similar gene expression pattern and comparable levels of inflammatory-associated genes (Figures S2L and 2J) that were differentially expressed between WT and β-catenin-deficient AMs (Figure 2D). To further confirm that the loss of β-catenin in tissue-resident macrophages, rather than circulating monocytes, monocyte-derived macrophages (MdMs), and/or neutrophils, regulates IAV-induced pulmonary inflammation, we performed parabiosis and joined the blood vessels of *Ctnnb1*$^{fl/fl}$ and *Ctnnb1*$^{\Delta Lyz2}$ mice (Figure 2K). We then infected *Ctnnb1*$^{fl/fl}$ and *Ctnnb1*$^{\Delta Lyz2}$ parabiotic mice with IAV and examined airway cytokines at 4 d.p.i. We observed decreased levels of IL-1β, TNF-α, CCL2, or IL-6 in BAL of *Ctnnb1*$^{\Delta Lyz2}$ mice compared to their parabiotic counterparts at 4 d.p.i. (Figure 2K). These data suggest that the decreased pulmonary inflammation observed in *Ctnnb1*$^{\Delta Lyz2}$ mice is possibly due to a cell-autonomous effect of β-catenin deficiency in tissue-resident macrophages rather than in circulating immune cells.

Tissue-resident interstitial macrophages and nerve- and airway-associated macrophages (NAMs) regulate pulmonary inflammation following IAV infection (Ural et al., 2020). However, NAMs expressed lower levels of *Ctnnb1* and had decreased active β-catenin following IAV infection than AMs (Figures S2N and S2O) (Ural et al., 2020). We next utilized *Ctnnb1*$^{\Delta CD11c}$ mice to ablate β-catenin in CD11c^{+} cells. CD11c is expressed in AMs and DCs, but not NAMs (Ural et al., 2020; Zhu et al., 2019). AMs sorted from IAV-infected *Ctnnb1*$^{\Delta CD11c}$ mice had diminished expression of a number of inflammation-related genes at 3 or 6 d.p.i. (Figure 2L). In accordance, *Ctnnb1*$^{\Delta CD11c}$ mice had diminished accumulation of inflammatory monocytes and neutrophils in the lung (Figure S3A). Importantly, *Ctnnb1*$^{\Delta CD11c}$ mice exhibited much milder weight loss (Figure 2M) with similar levels of adaptive T cell responses compared to *Ctnnb1*$^{fl/fl}$ mice (Figure S3B), suggesting that β-catenin deficiency in CD11c^{+} DCs did not impair their ability to induce protective T cell immunity. Taken together, our data on BM chimera, parabiosis, and selective β-catenin ablation in different structural and immune cells suggest that β-catenin expression in AMs is most likely responsible for the modulation of pulmonary inflammation and host diseases following IAV infection.

Interaction of β-catenin and HIF-1α promotes glycolysis-dependent AM inflammation

GSEA on the scRNA-seq data revealed that there was a significant enrichment of hypoxia gene set following Wnt3a treatment (Figure 3A). Notably, HIF-1α expression was upregulated in AMs with Wnt3a stimulation in a β-catenin-dependent manner (Figures 3B and S3C–S3E). HIF-1α signaling has been associated with macrophage inflammatory responses (Cramer et al., 2003; Tannahill et al., 2013). We therefore examined whether Wnt3a-induced AM inflammatory gene expression was dependent on HIF-1α. We treated WT or HIF-1α-deficient AMs (isolated from *Hif1a*$^{\Delta CD11c}$ mice) with Wnt3a and measured IL-1β, TNF-α, and CCL2 production. HIF-1α deficiency diminished the levels of those cytokines in AMs following Wnt3a treatment (Figure 3C), suggesting that β-catenin-dependent HIF-1α signaling was required for AM inflammation following Wnt ligand treatment.

We next compared the transcriptional profiles of WT AMs, WT AMs treated with Wnt3a, β-catenin-deficient AMs treated with Wnt3a, and HIF-1α-deficient AMs treated with Wnt3a. β-Catenin deficiency largely abolished the effects of Wnt3a treatment on AM transcription (Figure 3D). Strikingly, HIF-1α-deficient AMs essentially phenocopied those of β-catenin-deficient AMs (Figures 3D–3F), suggesting that the β-catenin-HIF-1α axis represents the major downstream pathway of Wnt signaling in AMs. We next sought to determine how HIF-1α activation in AMs change over time following IAV infection. *In vitro*, AM HIF-1α expression was upregulated at 24 and 48 h post-IAV infection (Figure S3F). *In vivo*, AM HIF-1α levels peaked at 6 d.p.i and then decreased at 10 and 15 d.p.i. (Figure 3G), which were correlative with active β-catenin levels in AMs upon IAV infection (Figures 2B and S2B). Furthermore, IAV-induced HIF-1α expression was compromised in β-catenin-deficient AMs at 6 and 8 d.p.i (Figure S3G). Additionally, most of the Wnt ligand genes

Figure 3. β-Catenin-HIF-1α complex promotes glycolysis-dependent AM inflammation

(A) GSEA of hypoxia gene set in AMs (as in Figure 1D).

(B) HIF-1α levels in AMs following Wnt3a treatment *in vivo* (n = 5).

(C) IL-1β, TNF-α, and CCL2 secretion of AMs with indicated genotypes and treatments *in vitro* (n = 3).

(D–F) RNA-seq analysis of cultured AMs with indicated genotypes and treatments. (D) Heatmap of differentially expressed genes (DEGs). (E) Venn diagram of DEGs from WT AMs treated with Wnt3a versus *Ctnnb1*$^{\Delta Lyz2}$ and *Hif1a*$^{\Delta CD11c}$ AMs treated with Wnt3a. (F) Heatmap showing differentially expressed cytokines.

(G) HIF-1α levels in AMs at indicated d.p.i. (n = 3 mice per group).

(H) NanoString analysis of inflammatory genes in AMs sorted from IAV-infected *Hif1a*$^{fl/fl}$ or *Hif1a*$^{\Delta CD11c}$ mice at indicated d.p.i.

(I–K) *Hif1a*$^{\Delta CD11c}$ or *Hif1a*$^{fl/fl}$ mice were infected with IAV. (I) Cytokine levels at 4 d.p.i. (n = 3). Host morbidity (J) and mortality (K) following infection.

(L) Coimmunoprecipitation (IP) was performed using β-catenin and HIF-1α Abs in AMs or B16 cell lines followed by western blotting (WB) for analysis of β-catenin, TCF-4, and HIF-1α interaction.

(M) ChIP analysis of β-catenin and HIF-1α binding to *Il1b*, *Cxcl1*, *Eno1*, *Hk2*, and *Slc2a1* loci in AMs treated with Wnt3a.

(N) Extracellular acidification rate (ECAR) analysis of AMs with indicated genotypes and treatments (n = 6). 1, glucose; 2, oligomycin; and 3, 2-DG.

(O) IL-1β, TNF-α, and CCL2 secretion in WT AMs treated with indicated conditions (n = 3).

Representative or pooled data (J, K, M, and N) from at least two independent experiments (except A, D–F, and H). Data are the mean ± SEM. *, $p < 0.05$; **, $p < 0.01$. See also Figure S3.

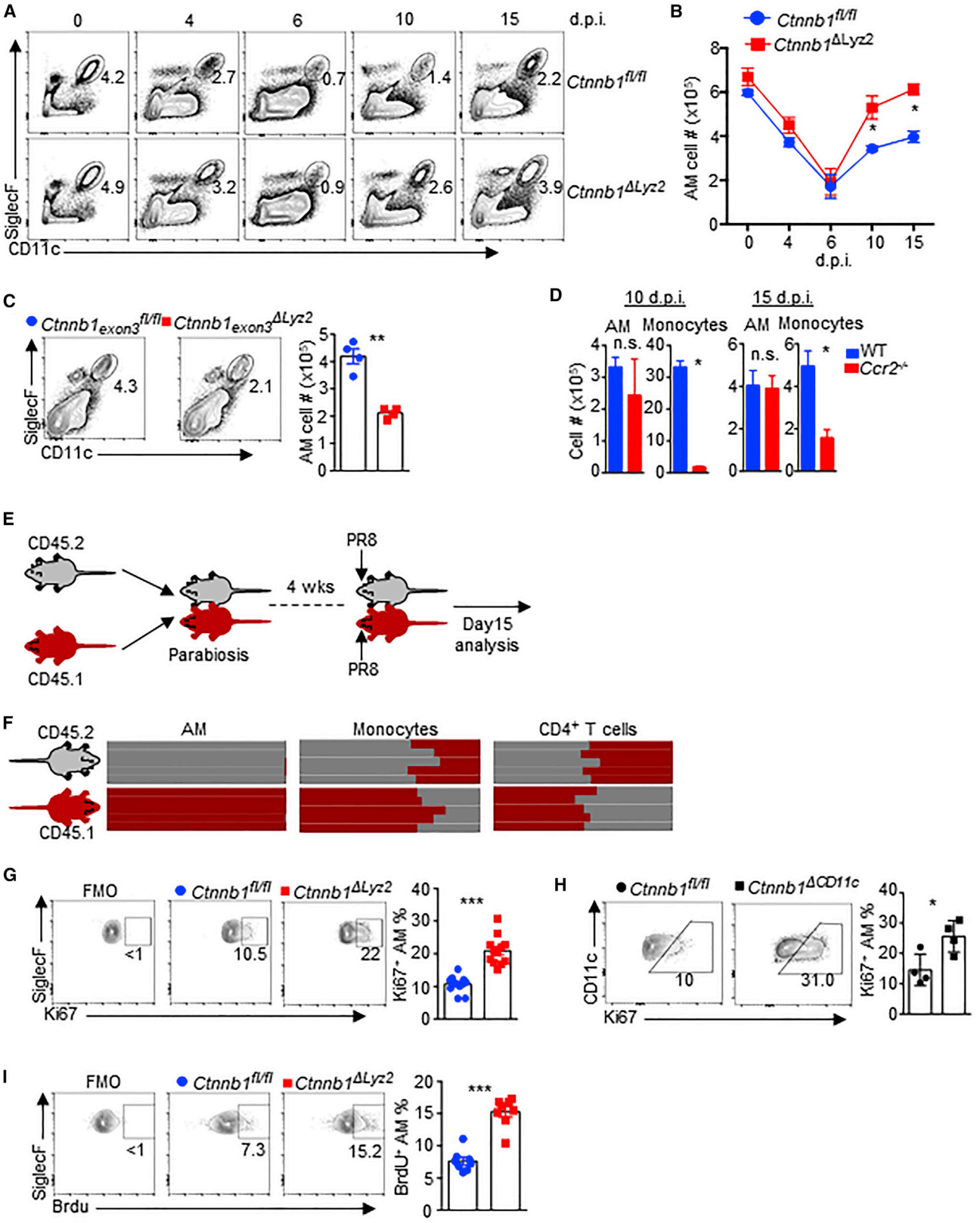

(legend on next page)

that were upregulated following IAV infection remained unchanged in HIF-1α-deficient AMs, while some genes (such as *Wnt2b*, *Axin2*, or *Tcf7l2*) showed differentially expressed in HIF-1α-deficient AMs at ~24 h post-infection. compared to WT AMs (Figure S3H). Taken together, these data indicated that IAV infection likely induced Wnt ligands expression first, resulting in the subsequent activation of Wnt/β-catenin signaling and HIF-1α in AMs.

HIF-1α deficiency led to diminished expression of inflammatory-associated genes in AMs at 3 or 6 d.p.i. (Figure 3H and S3I), suggesting that the loss of HIF-1α diminished AM inflammatory responses following IAV infection. Furthermore, the absence of HIF-1α in CD11c$^+$ cells decreased the production of inflammatory cytokines as well as diminished accumulation of inflammatory immune cells, including neutrophils and monocytes in the respiratory tract (Figures 3I and S3J). The decreased accumulation of inflammatory immune cells in the lung following IAV infection could be due to the diminished chemokine expression (such as *Ccl2* and *Cxcl10*) in HIF-1α-deficient AMs (Figure 3H). Consequently, HIF-1α-deficient mice had enhanced body weight recovery, decreased mortality, and enhanced body temperature recovery upon IAV infection (Figures 3J and 3K and S3L) compared to those of WT mice, but the kinetics and magnitude of lung CD4$^+$ or CD8$^+$ T cell responses were similar between *Hif1a*$^{\Delta CD11c}$ and *Hif1a*$^{fl/fl}$ mice (Figures S3K). These data indicate that Wnt/β-catenin signaling promotes AM inflammatory activities through HIF-1α, thereby regulating pulmonary inflammation and host morbidity following IAV infection.

β-Catenin and HIF-1α are reported to bind to each other in cancer cell lines under hypoxic conditions (Kaidi et al., 2007), although little is known about their possible interaction under normoxia condition. We performed coimmunoprecipitation assays with antibody (Ab) to β-catenin and revealed that β-catenin complexed with TCF-4 in AMs without Wnt3a stimulation (Figure 3L). Following Wnt3a engagement, β-catenin bound to HIF-1α instead of TCF-4 (Figure 3L). Similarly, the reverse precipitation using HIF-1α Ab showed HIF-1α interacted with β-catenin, but not TCF-4, in Wnt3a-treated AMs (Figure 3L). These data suggest that HIF-1α competes with TCF-4 for β-catenin binding in AMs following Wnt ligand engagement. Notably, β-catenin interacted with TCF-4, but not HIF-1α, in B16 cancer cell lines in the presence of Wnt3a (Figure 3L), suggesting that the interaction of β-catenin and HIF-1α in AMs under normoxia condition was cell-type specific. Together, these data suggest that Wnt3a triggers the formation of β-catenin and HIF-1α transcriptional complex, which may promote and/or repress downstream gene expression. In support of this idea, β-catenin and HIF-1α bound the same region of certain proinflammatory genes, such as *Il1b* and *Cxcl1*, as identified by chromatin immunoprecipitation (ChIP) (Figure 3M).

HIF-1α is known to promote cell glycolytic metabolism, which is needed for the inflammatory capacity of macrophages (Caputa et al., 2019; Cheng et al., 2014; Cramer et al., 2003; Tannahill et al., 2013). Consistently, core glycolytic genes were upregulated in AMs following Wnt3a treatment in a β-catenin- and HIF-1α-dependent manner (Figure S3M), and certain genes, such as *Eno1*, *Hk2*, and *Slc2a1*, were directly regulated by β-catenin and HIF-1α (Figure 3M). Consequently, Wnt3a stimulation led to elevated AM glycolytic capacity, which was abrogated following β-catenin and HIF-1α deficiency (Figures 3N, S3N, and S3O). Importantly, pharmacological inhibition of glycolysis by 2-deoxyglucose (2-DG) suppressed Wnt3a-induced inflammatory cytokine production in AMs (Figure 3O). These results indicate that Wnt-β-catenin promotes AM inflammation through the regulation of HIF-1α-driven glycolysis.

β-Catenin controls AM proliferation and repopulation following partial depletion during IAV infection

Following the establishment of β-catenin in mediating AM inflammatory activities, we next sought to examine whether β-catenin signaling regulates AM proliferation and/or self-renewal *in vivo*. Myeloid or CD11c$^+$ cell β-catenin deficiency appeared to not affect AM development or proliferation under steady state (Figures 4A, 4B, and S4A–S4E). As shown before (Aegerter et al., 2020; Ghoneim et al., 2013; Hashimoto et al., 2013; Machiels et al., 2017; Misharin et al., 2017), IAV infection partially depleted AMs (defined as CD11c$^+$ SiglecF^{hi}) at the peak of inflammation (6 d.p.i.) in both *Ctnnb1*$^{fl/fl}$ and *Ctnnb1*$^{\Delta Lyz2}$ mice (Figures 4A, 4B, and S4C). AMs were then repopulated concomitant with the resolution of inflammation, possible via local proliferation and/or monocyte differentiation, at 10 and 15 d.p.i. (Figures 4A, 4B, and S4C) (Aegerter et al., 2020; Hashimoto et al., 2013). Notably, β-catenin-deficient mice (*Ctnnb1*$^{\Delta Lyz2}$ or *Ctnnb1*$^{\Delta CD11c}$) exhibited enhanced AM repopulation (Figures 4A, 4B, and S4C), whereas constitutive activation of β-catenin in mice (*Ctnnb1*$_{exon3}$$^{\Delta Lyz2}$ mice) diminished AM regeneration following IAV infection (Figure 4C).

Monocytes can differentiate into AMs during inflammation and diseases, but the extent of monocyte contribution to AM repopulation varies in different models (Aegerter et al., 2020; Hashimoto et al., 2013; Machiels et al., 2017; Yao et al., 2018). Monocytes have been shown to contribute significantly to AMs 4 weeks following IAV infection (Aegerter et al., 2020); however, whether monocytes contribute significantly to AM repopulation during the first 2 weeks of IAV infection is undetermined. Notably, *Ccr2*$^{-/-}$ mice had greatly diminished monocyte infiltration to

Figure 4. AMs are partially reduced upon IAV infection and repopulated via local proliferation

(A and B) *Ctnnb1*$^{fl/fl}$ or *Ctnnb1*$^{\Delta Lyz2}$ mice were infected with IAV (n = 5–7). Percentage (A) and number (B) of AMs at indicated d.p.i.

(C) AM number of *Ctnnb1*$_{exon3}$$^{fl/fl}$ or *Ctnnb1*$_{exon3}$$^{\Delta Lyz2}$ mice (n = 4) at 15 d.p.i.

(D) Lung AM and monocyte number from IAV-infected WT or *Ccr2*$^{-/-}$ mice (n = 4).

(E and F) Schematics of parabiosis and IAV infection (n = 5 pairs) (E). Percentage of partner cells in AMs, monocytes, and CD4$^+$ T cells in the lung at 15 d.p.i. (F).

(G) Percentage of Ki67$^+$ AMs from *Ctnnb1*$^{fl/fl}$ or *Ctnnb1*$^{\Delta Lyz2}$ mice at 8 d.p.i. (n = 12).

(H) Percentage of Ki67$^+$ AMs from *Ctnnb1*$^{fl/fl}$ or *Ctnnb1*$^{\Delta CD11c}$ mice at 8 d.p.i. (n = 4).

(I) Percentage of BrdU$^+$ AMs from *Ctnnb1*$^{fl/fl}$ or *Ctnnb1*$^{\Delta Lyz2}$ mice at 8 d.p.i. (n = 8).

Representative or pooled data (A, B, E–G, and I) from at least two independent experiments. Data are the mean ± SEM. *, $p < 0.05$; **, $p < 0.01$; ***, $p < 0.001$. See also Figure S4.

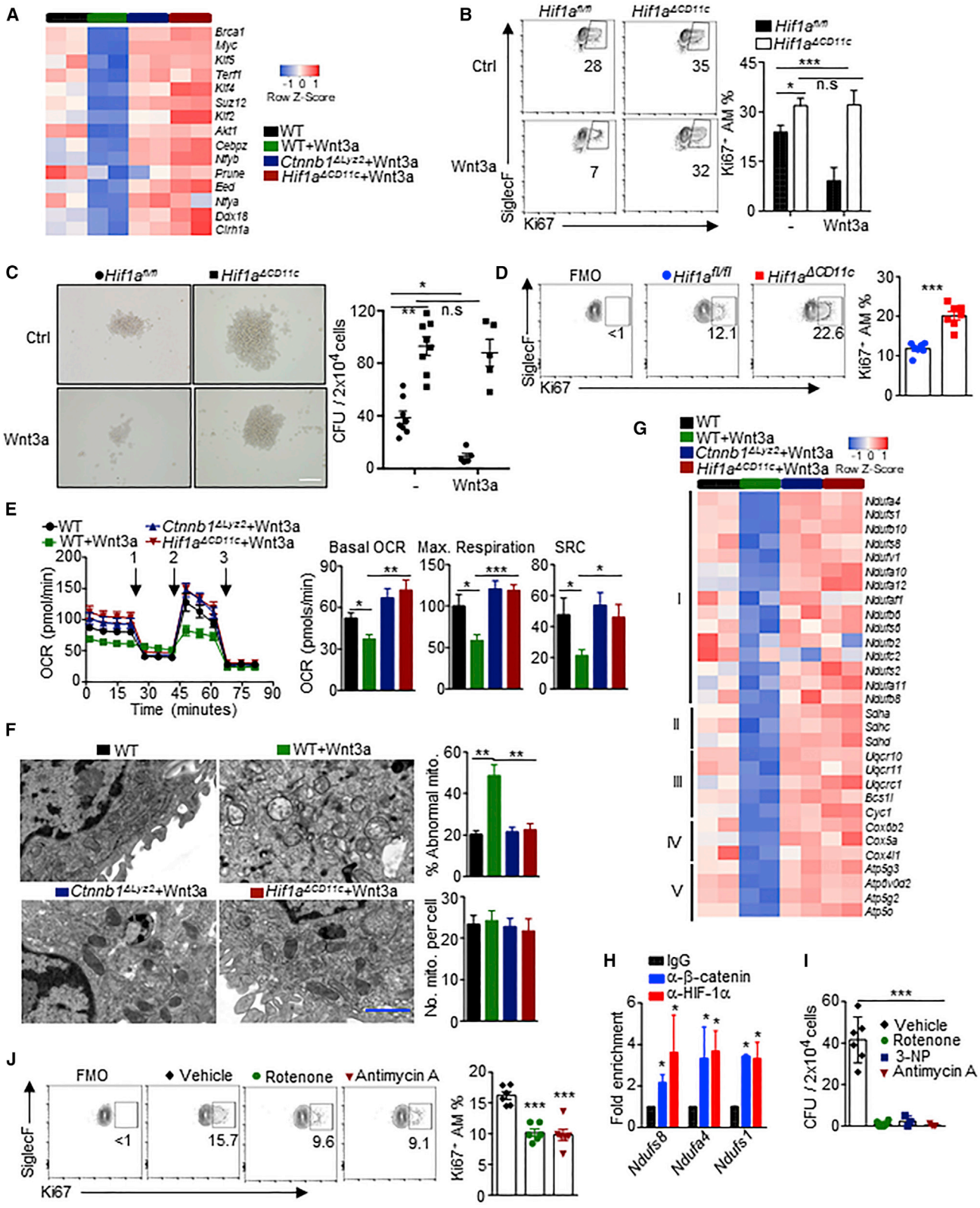

Figure 5. The β-catenin-HIF-1α axis suppresses AM self-renewal by impairing mitochondrial fitness

(A) Self-renewal gene levels in AMs with indicated genotypes and treatments.

(B) Percentage of Ki67$^+$ AMs with indicated genotypes and treatments (n = 4).

(C) CFUs of AMs with indicated genotypes and treatments (n = 5–8). Scale bars, 200 μm.

(legend continued on next page)

the lungs but comparable AM numbers compared to WT mice at 10 or 15 d.p.i. (Figure 4D), suggesting that AM repopulation during the inflammation resolution phase could be largely independent of monocytes. In a complementary approach, we transferred total CD45.1$^+$ BM cells into IAV-infected *Ccr2*$^{-/-}$ mice at 6 d.p.i. and monitored the engraftment of donor cells into the lung at 14 (acute phase) and 46 (memory phase) d.p.i. The percentage of CD45.1$^+$ donor cells in AMs was negligible at 14 d.p.i. compared to noticeable AMs differentiated from monocytes at 46 d.p.i. (Figures S4A and S4F). These data suggest that circulating hematopoietic monocytes or monocyte progenitors contribute to the AM pool at the memory stage but moderately give rise to AMs at the acute stage of IAV infection.

We next parabiotically joined CD45.2$^+$ and congenic CD45.1$^+$ mice for 4 weeks. Following the confirmation of successful blood circulation (Figures S4B and S4G), we infected both parabiotic mice with IAV (Figure 4E). At 15 d.p.i., the lungs of parabiotic mice contained approximately equivalent numbers of CD4$^+$ T cells, and ~30% of monocytes derived from the parabiotic partners (Figures 4F, S4A, and S4H). However, <2% of partner AMs were observed in the respective lungs of parabionts at 15 d.p.i. (Figures 4F and S4H). The data confirmed that circulating monocytes only moderately contributed to AM repopulation during acute IAV infection. Given the relatively small contributions of monocytes into AM compartment, we hypothesized that β-catenin regulates AM repopulation mainly through its regulation of AM proliferation *in vivo*. Consistent with the hypothesis, there were increased percentages of Ki67$^+$ AMs from *Ctnnb1*$^{\Delta Lyz2}$ or *Ctnnb1*$^{\Delta CD11c}$ mice compared to those of WT mice at 8 d.p.i. (Figures 4G and 4H). Furthermore, β-catenin deficiency (*Ctnnb1*$^{\Delta Lyz2}$ mice) resulted in a significant increase in bromodeoxyuridine (BrdU) incorporation in AMs at 8 d.p.i. (Figure 4I). Together, these data indicate that β-catenin signaling potently inhibits AM proliferation *in vivo* to restrict "immediate" AM repopulation following their partial depletion during IAV infection.

The β-catenin-HIF-1α axis controls AM proliferation and repopulation through disruption of mitochondrial fitness

Wnt3a treatment inhibited macrophage self-renewal gene expression (Soucie et al., 2016), Ki67 expression, and colony-forming ability of AMs in a HIF-1α-dependent fashion (Figures 5A–5C). Further, AM proliferation was inhibited under hypoxic conditions (Figure S5A), suggesting that hypoxia-induced HIF-1α activation suppressed AM proliferation. Additionally, loss of HIF-1α increased Ki67 expression in AMs at 8 d.p.i., but not at the steady state (Figures 5D, S5B, and S5C). Thus, HIF-1α activation suppresses AM self-renewal *in vitro* and *in vivo*, which is consistent with a recent report demonstrating that Von Hippel-Lindau protein (*Vhl*) (a negative regulator of HIF transcription factors) is important for AM proliferation (Izquierdo et al., 2018).

2-DG, which abrogated the inflammatory activities of AMs following Wnt3a treatment (Figure 3O), did not alter AM proliferative capability with or without Wnt3a treatment (Figure S5D), indicating glycolysis was dispensable for modulation of AM proliferation. We next measured mitochondrial oxidative phosphorylation (OXPHOS) in AMs from *Ctnnb1*$^{fl/fl}$, *Ctnnb1*$^{\Delta Lyz2}$, *Hif1a*$^{fl/fl}$ or *Hif1a*$^{\Delta CD11c}$ mice. The oxygen consumption rate (OCR) was similar in AMs from the different mouse strains without Wnt ligand treatment (Figure S5E). However, following Wnt3a treatment, the mitochondrial respiration was significantly reduced in Wnt3a-treated AMs in a β-catenin- and HIF-1α-dependent manner (Figure 5E). We then performed transmission electron microscopy (EM) to examine AM mitochondrial morphology with or without Wnt3a treatment. Wnt3a stimulation resulted in impaired cristae formation and swollen mitochondria (Figure 5F), reflective of increased mitochondria damage (Li et al., 2019; Sohn et al., 2013). Strikingly, β-catenin or HIF-1α deficiency abrogated the effects of Wnt3a on mitochondrial morphology (Figure 5F). Consistently, in the *in vivo* model, IAV infection disrupted mitochondria morphology in sorted WT AMs at 8 d.p.i. (Figure S5F). Loss of β-catenin or HIF-1α rescued the damaged mitochondria of AMs sorted from virus-infected mice (Figure S5F), suggesting that the β-catenin-HIF-1α axis in AMs inhibited mitochondrial fitness *in vivo*. Consistent with the findings that β-catenin-HIF-1α signaling impaired mitochondrial fitness *in vitro* and *in vivo*, Wnt triggered β-catenin-HIF-1α activation suppressed mitochondrial electron transport chain (ETC) gene expression (Figure 5G). Further, ChIP analysis confirmed that HIF-1α and β-catenin can bind to several mitochondrial genes (Figure 5H).

We next tested the roles of mitochondrial metabolism in AM proliferation and self-renewal. Blockade of complexes I, II, and III by rotenone, 3-Nitropropionic acid (3-NP), and antimycin A, respectively resulted in a decreased Ki67 and cyclin B1 expression as well as inhibition of colony formation in AMs *in vitro* (Figures 5I, S5G, and S5H). Furthermore, treatment of WT mice with rotenone and antimycin A suppressed AM proliferation *in vivo* (Figure 5J). Together, our data suggest that Wnt signaling through β-catenin and HIF-1α impairs mitochondrial function and fitness, thereby inhibiting AM proliferation and self-renewal.

HIF-1α activity determines AM inflammatory versus proliferative fate choice *in vivo*

Both active β-catenin and HIF-1α levels peaked at 6 d.p.i. (Figures 2B and 3G). The reduction of active β-catenin and HIF-1α levels were associated with diminished inflammatory activities

(D) Percentage of Ki67$^+$ AMs from *Hif1a*$^{fl/fl}$ or *Hif1a*$^{\Delta CD11c}$ mice (n = 8) at 8 d.p.i.
(E) OCR of AMs with indicated genotypes and treatments (n = 6). 1, oligomycin; 2, carbonyl cyanide-4-(trifluoromethoxy) phenylhydrazone (FCCP); and 3, antimycin A/rotenone.
(F) EM images of AMs with indicated genotypes and treatments (n = 3). Scale bar, 0.5 μm. Right: mitochondrial number and percentage of abnormal mitochondria in AMs.
(G) Differentially expressed ETC genes in AMs with indicated genotypes and treatments.
(H) ChIP analysis of β-catenin and HIF-1α binding to *Ndufs8*, *Nufa4*, and *Ndufs1* loci in AMs treated with Wnt3a.
(I) CFU of WT AMs treated with vehicle, rotenone, 3-NP, or antimycin A (n = 3–6).
(J) IAV-infected WT mice were administered with rotenone or antimycin A at 7 d.p.i. % Ki67$^+$ AMs at 8 d.p.i. (n = 6).
Representative or pooled data (C–E and J) from at least two independent experiments (except A and G). Data are the mean ± SEM. *, $p < 0.05$; **, $p < 0.01$; ***, $p < 0.001$. See also Figure S5.

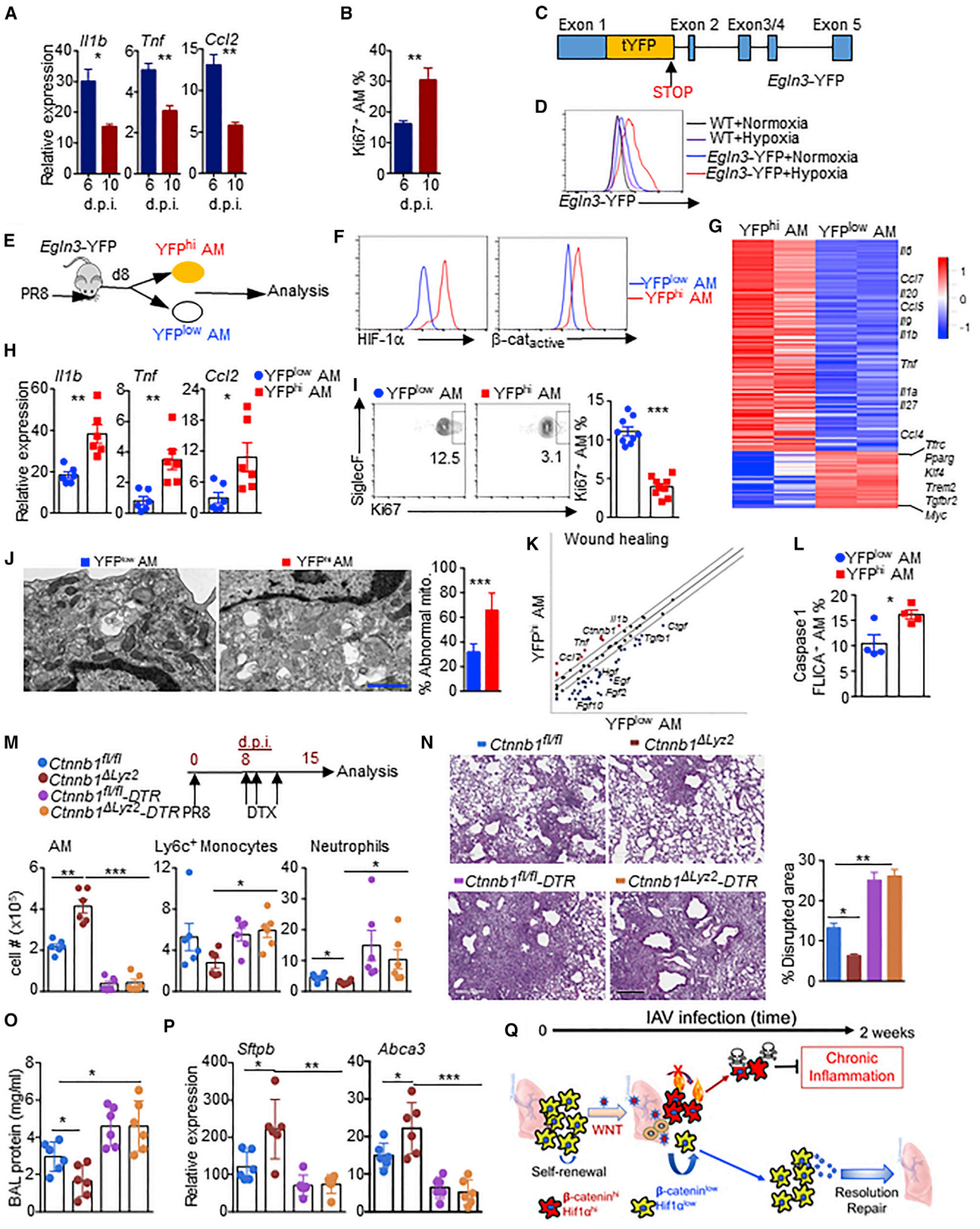

(legend on next page)

and increased proliferative capability in AMs at 10 d.p.i. (Figures 6A and 6B). In addition to their anti-viral and inflammatory functions, AMs are vital for wound healing and tissue repair following injury (Hussell and Bell, 2014; Minutti et al., 2017). To this end, AMs at 10 d.p.i. showed enhanced expression of wound-healing genes measured by RT^2 profiler qRT-PCR array compared to those at 6 d.p.i. (Figure S5I). These data suggest that AMs appear to transit from inflammation-prone activities at the peak of pulmonary inflammation to proliferative and reparative activities at the resolution phase during the course of IAV infection.

We sought to determine the underlying cellular mechanisms that may explain the transition of inflammatory AMs to pro-proliferation or pro-repair AMs. Our *in vitro* scRNA-seq data revealed that when Wnt3a-treated AMs were divided into *Hif1a*^{hi} and *Hif1a*^{low} AMs, there was a significant enrichment of inflammatory gene sets in *Hif1a*^{hi} AMs (Figure S5J). In contrast, *Hif1a*^{low} AMs were enriched for E2F, Myc, and ESC gene modules (Figure S5J), which were associated with AM proliferation and self-renewal. Therefore, we hypothesized that AMs may exhibit potent heterogeneity *in vivo* separated by β-catenin and HIF-1α transcriptional activities. To test this, we utilized novel HIF-1α activity reporter mice, *Egln3*-YFP mice, in which YFP served as transcriptional reporter of *Egln3* mRNA (Figure 6C). *Egln3* belongs to the HIF prolyl hydroxylase domain family (PHD) of proteins and is a direct target for HIF-1α-mediated transcription (del Peso et al., 2003); thus, YFP expression in cells indicates HIF-1α activity. The mice were bred as *Egln3*$^{YFP/+}$ to minimize potential *Egln3*-dependent phenotypes.

To produce enough mice for experiments, we generated BM chimeric mice by transplantation of BM from *Egln3*-YFP mice into lethally irradiated WT C57BL/6 mice. Ten weeks following AM regeneration, we analyzed HIF-1α activity. We first confirmed hypoxia-dependent enhancement of YFP expression in AMs *in vitro* (Figure 6D). *In vivo*, IAV infection-induced YFP expression in AMs and peaked at 6 d.p.i. (Figure S5K), similar to HIF-1α expression (Figure 3G). We then sorted YFP^{hi} and YFP^{low} AMs from viral infected mice at 8 d.p.i. (Figures 6E and S5L). YFP^{hi} AMs had enhanced expression of HIF-1α, which was concomitant with the upregulation of active β-catenin compared to YFP^{low} AMs (Figure 6F). Notably, a number of cytokines/chemokines were upregulated in YFP^{hi} AMs, whereas genes related to anti-inflammatory activity or cell proliferation were elevated in YFP^{low} AMs (Figures 6G and 6H). Further, YFP^{low} AMs exhibited enhanced Ki67 expression compared to YFP^{hi} AMs (Figure 6I). Of note, the majority of AMs are monocyte derived in BM chimeric mice, which might exhibit different phenotypes compared to the resident AMs in nonirradiated mice. To further confirm whether resident AM inflammatory activities and proliferation were determined by HIF-1α activity *in vivo*, we sorted YFP^{hi} and YFP^{low} AMs from IAV-infected *Egln3*-YFP mice (without irradiation) at 6 and 10 d.p.i. Consistently, YFP^{hi} AMs exhibited higher levels of HIF-1α and active β-catenin, increased expression of inflammatory cytokines, and diminished Ki67 levels compared to YFP^{low} AMs (Figures S5M, S6A, and S6B).

YFP^{low} AMs had lower levels of damaged mitochondria (Figure 6J), which may explain the higher proliferative capacity in YFP^{low} AMs. YFP^{low} AMs also upregulated the expression of wound-healing genes (Figure 6K), indicating that YFP^{low} AMs are more reparative than YFP^{hi} AMs. In order to determine the cell fate of YFP^{hi} and YFP^{low} AMs during the resolution phase of lung inflammation, we assessed active caspase-1 and annexin V staining on AMs. YFP^{hi} AMs appeared to be more susceptible to apoptosis/pyroptosis (Figures 6L, S6C, and S6D). Thus, YFP^{hi} AMs had limited proliferation and increased cell death, while YFP^{low} AMs showed enhanced proliferation, which may be needed for the repopulation of reparative AMs for inflammation resolution and/or lung repair during the recovery phase of IAV infection. Taken together, our data suggest that HIF-1α activity uncouples AM inflammatory activities and progeny production *in vivo* during IAV infection.

Repopulation of reparative AMs facilitates inflammation resolution and tissue recovery

β-Catenin or HIF-1α deficiency in myeloid or CD11c$^+$ cells (*Ctnnb1*$^{\Delta Lyz2}$, *Ctnnb1*$^{\Delta CD11c}$, or *Hif1a*$^{\Delta CD11c}$ mice) had significantly diminished disrupted alveolar areas, decreased numbers of BAL inflammatory monocytes and neutrophils, and lowered BAL protein levels at 15 d.p.i. (Figures S6E–S6L). Furthermore, ATII-cell-specific genes, including *Sftpb* and *Abca3*, were significantly elevated in the lungs of myeloid- or CD11c$^+$-cell-specific β-catenin- or HIF-1α-deficient mice (Figures S6G, S6J, and S6O). These data indicate that enhanced repopulation of reparative AM following β-catenin or HIF-1α deficiency may facilitate inflammation resolution and prompt tissue recovery from IAV infection. To directly test this idea, we depleted CD169$^+$ resident macrophages (Hashimoto et al., 2013; Purnama et al., 2014; Ural

Figure 6. Inflammatory and proliferative AMs are separated by HIF-1α activity *in vivo*

(A) *Il1b*, *Tnf*, and *Ccl2* levels in AMs at 6 or 10 d.p.i. (n = 3).

(B) Percentage of Ki67$^+$ AMs that were isolated from IAV-infected mice (6 or 10 d.p.i.) and cultured with GM-CSF *in vitro*.

(C) Schematic of *Egln3*-YFP transgenic mice.

(D) YFP levels of WT or *Egln3*-YFP AMs exposed to hypoxia versus normoxia.

(E–K) *Egln3*-YFP mice were infected with IAV for 8 days. YFP^{low} and YFP^{hi} AMs were sorted as in Figure S5L. (E) Experimental design. (F) HIF-1α and active β-catenin expression in sorted AMs. (G) NanoString analysis of immune-related genes. (H) *Il1b*, *Tnf*, and *Ccl2* expression in AMs (n = 6). (I) Percentage of Ki67$^+$ AMs (n = 9). (J) EM images of YFP^{low} or YFP^{hi} AMs. Scale bar, 0.5 μm. Right, percentage of abnormal mitochondria in AMs. (K) Wound-healing gene expression in YFP^{low} AMs or YFP^{hi} AMs by PCR array (pooled from six mice). Dotted line indicates 2-fold difference. Red dots indicate genes upregulated in YFP^{hi} AMs. Blue dots indicate genes downregulated in YFP^{hi} AMs. (L) % active caspase-1$^+$ in YFP^{low} or YFP^{hi} AMs (n = 4).

(M–P) *Ctnnb1*$^{fl/fl}$, *Ctnnb1*$^{\Delta Lyz2}$, *Ctnnb1*$^{fl/fl}$-*CD169DTR* or *Ctnnb1*$^{\Delta Lyz2}$-*CD169DTR* mice (n = 6) were infected with IAV. (M) Diagram of DTX injection (upper) and number of AMs, monocytes, and neutrophils in the lungs (lower). (N) H&E staining of lung sections (left). Scale bar, 200 μm. Right, percentage of disrupted alveolar area. (O) BAL protein levels. (P) Lung *Sftpb* and *Abca3* expression.

(Q) Diagram of the model.

Representative or pooled data (H, I, M, O, and P) from two to three independent experiments (except G). Data are the mean ± SEM. *, $p < 0.05$; **, $p < 0.01$; ***, $p < 0.001$. See also Figures S5 and S6.

et al., 2020), in which AMs were the vast majority, during their repopulation at the recovery stage starting from 8 d.p.i. by utilizing mice expressing CD169-diphtheria toxin receptor (CD169-DTR/*Ctnnb1*$^{fl/fl}$ or CD169-DTR/*Ctnnb1*$^{\Delta Lyz2}$ mice) (Figure 6M). Short-term DTX administration into mice resulted in efficient depletion of AMs without affecting CD11b^{+} monocytes/macrophages, specifically in CD169-DTR/*Ctnnb1*$^{fl/fl}$ or CD169-DTR/*Ctnnb1*$^{\Delta Lyz2}$ mice, but not *Ctnnb1*$^{fl/fl}$ or *Ctnnb1*$^{\Delta Lyz2}$ mice (Figures 6M and S6P). AM depletion at the repopulation stage resulted in pronounced inflammation and impaired lung recovery, as evidenced by enhanced lung damage and augmented BAL protein concentration as well as reduced ATII gene expression in the lung of CD169-DTR/*Ctnnb1*$^{fl/fl}$ mice compared to mice lack CD169-DTR (*Ctnnb1*$^{fl/fl}$) at day 15 p.i. (Figures 6N–6P). Of note, the depletion of AMs in CD169-DTR/*Ctnnb1*$^{\Delta Lyz2}$ mice abrogated the effects of β-catenin deficiency in promoting tissue repair and inflammation resolution (Figures 6N–6P). Together, these data suggest that repopulation of reparative AM progenies is required for modulation of pulmonary inflammation and tissue recovery from IAV infection (Figure 6Q).

β-Catenin-HIF-1α function is conserved in human AMs and severe SARS-CoV-2 infection leads to increased macrophage HIF-1α expression

Next, we analyzed human AMs isolated from BAL of subjects free of inflammation and/or pulmonary infection (healthy sample). Consistent with the mouse data, Wnt3a treatment upregulated active β-catenin and HIF-1α expression and resulted in suppression of AM proliferation, as reflected by Ki67 staining (Figures 7A, 7B, S7A, and S7B). Of note, the suppression was at least partially restored by the HIF-1α pharmacological inhibitor LW6 (Figure 7B), which promoted proteasomal degradation of HIF-1α and thus decreased expression of HIF-1α (Figure 7A) (Lee et al., 2010). Furthermore, Wnt3a treatment resulted in increased expression of *IL1B*, *TNF*, and *CCL2* in AMs, but this upregulation was abolished in the presence of LW6 (Figure 7C). Thus, Wnt/β-catenin signaling through HIF-1α suppresses human AM proliferation and simultaneously promotes inflammatory activities of human AMs.

We then analyzed a publicly available microarray data containing the transcriptional profile of AMs that were infected with IAV *in vitro* for 24 h (Wang et al., 2011). IAV infection led to enhanced expression of a number of genes associated with Wnt ligands and signaling and diminished the expression of ESC gene module and macrophage self-renewal genes in human AMs (Figures S7C–S7E). Notably, inflammatory response and hypoxia pathway gene sets were enriched in IAV-infected AMs compared to control AMs (Figure S7D). Similar to IAV infection, SARS-CoV-2 infection, which causes coronavirus disease 2019 (COVID-19), results in profound macrophage inflammation in the lower respiratory tract (Tay et al., 2020). We made use of a publicly available set of scRNA-seq data on BAL cells from patients with moderate or severe SARS-CoV-2 infection and healthy controls (GEO: GSE145926; Liao et al., 2020). SARS-CoV-2 infection enhanced the expression of a number of Wnt ligands in BAL cells from patients with COVID-19 compared to healthy BAL cells (Figure 7D), suggesting that SARS-CoV-2 infection may activate Wnt signaling *in vivo*. A total of 20 CD68^{+} macrophages clusters were identified showing distinct separation by UMAP in our analysis (Figure S7F). According to the previous study (Liao et al., 2020), the 20 clusters were assigned into two groups: *FABP4*$^{+}$ tissue-resident AM group and *FCN1*$^{+}$ MdM group (Figure S7F). There were 17,981 AMs and 129 MdMs in healthy donors, 3,736 AMs and 449 MdMs in mild COVID-19 patients, and 2,184 AMs and 25,418 MdMs in severe COVID-19 patients. Of note, *HIF1A* was highly expressed in AMs of patients with severe COVID-19 compared to AMs of mild COVID-19 patients and healthy donors (Figure 7E). Further, hypoxia and inflammatory response gene modules were enriched in AMs of severe COVID-19 patients in contrast to healthy AMs (Figures 7F and S7G), while there was a significant enrichment of self-renewal gene sets in healthy AMs over AMs from severe SARS-CoV-2-infected patients (Figures 7F and S7G).

MdMs is a major cell type responsible for severe COVID-19 inflammation (Liao et al., 2020; Merad and Martin, 2020; Tay et al., 2020). To this end, upregulation of *HIF1A* expression and enrichment of hypoxia and inflammatory response gene sets were observed in MdMs following severe SARS-CoV-2 infection (Figures S7H–S7J). A recent paper suggested that recruited MdMs may also undergo *in situ* proliferation during respiratory viral infection (Pernet et al., 2019). Consistently, there was an enrichment of ESC, Myc target, and OXPHOS gene sets in healthy MdMs compared to those of MdMs in severe SARS-CoV-2 infection (Figures S7I and S7J). These data suggested that HIF-1α activities may separate proliferation and inflammatory activity in both resident and recruited macrophages in the context of COVID-19.

Inhibition of HIF-1α mitigates severe inflammation and accelerates recovery following viral pneumonia

Notably, conventional β-catenin signaling is required for epithelial stem cell function following lung injury, while epithelial HIF-1α deletion may promote lung recovery (Xi et al., 2017). Therefore, we reasoned that the inhibition of HIF-1α, but not β-catenin, may be promising for treatment of respiratory viral diseases. To this end, LW6 treatment resulted in diminished host morbidity and mortality and enhanced body temperature recovery following IAV infection (Figures 7G, 7H, and S7K). Further, LW6 treatment decreased proinflammatory cytokine production in airway and lowered accumulation of inflammatory monocytes and neutrophils at 4 d.p.i. (Figures 7I and S7L). Additionally, inhibition of HIF-1α enhanced AM repopulation, reduced disrupted alveolar areas, decreased BAL inflammatory cell and protein levels, and promoted lung *Abca3* and *Sftpb* gene expression at day 14 p.i., (Figures 7J–7L and S7M). These data indicate that inhibition of HIF-1α ameliorates severe pulmonary inflammation and facilitates tissue recovery from viral pneumonia. Thus, HIF-1α may represent a potential therapeutic target for severe respiratory viral diseases, including COVID-19.

DISCUSSION

Wnt-β-catenin-TCF-4 signaling in DCs promotes anti-inflammatory cytokine production, thereby mediating gut mucosal tolerance (Manicassamy et al., 2010; Manoharan et al., 2014; Suryawanshi et al., 2016). In contrast, we found that Wnt-β-catenin signaling potently induced a variety of proinflammatory gene expression in AMs, causing exaggerated pulmonary inflammation

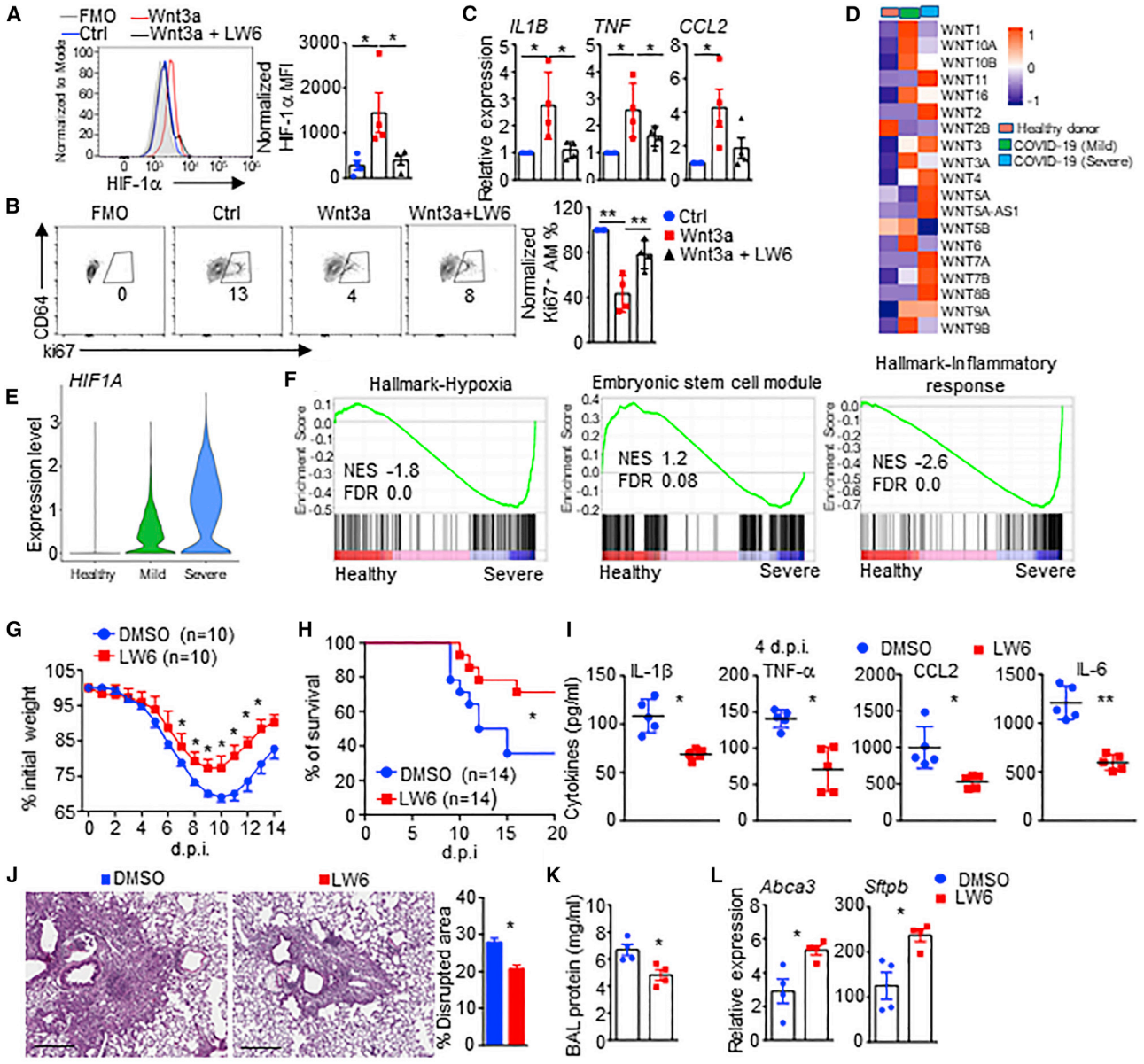

Figure 7. Wnt-β-catenin-HIF-1α signaling is conserved in human AMs and may contribute to severe disease during COVID-19

(A–C) Human AMs were treated with indicated conditions. (A) AM HIF-1α expression. (B) Percentage of Ki67$^+$ AMs. (C) *IL1B, TNF*, and *CCL2* expression.

(D–F) scRNA-seq dataset (GSE145926) on BAL cells from healthy controls and patients with moderate or severe COVID-19. (D) Differentially expressed Wnt ligands. (E) *HIF1A* expression. (F) GSEA of AMs from health donors or severe COVID-19 patients with indicated gene sets.

(G–L) WT mice were infected with IAV and treated with DMSO or LW6. Host morbidity (G) and mortality (H). (I) BAL cytokine levels at 4 d.p.i. (J) H&E staining of lung sections (n = 4). Scale bar, 200 μm. Right, percentage of disrupted alveolar area at 14 d.p.i. (K) BAL protein levels at 14 d.p.i. (L) Lung *Abca3* and *Sftpb* expression at 14 d.p.i.

Representative or pooled data (G and H) from two to three independent experiments. Data are the mean ± SEM. *, $p < 0.05$; **, $p < 0.01$. See also Figure S7.

following viral infection through HIF-1α. It is possible that the pro- or anti-inflammatory effects of Wnt-β-catenin signaling in different immune cells are determined by the differential binding partners of β-catenin (i.e., TCF-4 versus HIF-1α). Additionally, Wnt/β-catenin signaling normally promotes the self-renewal of stem cells, including lung epithelial stem cells (Clevers and Nusse, 2012; Nabhan et al., 2018; Rajagopal et al., 2008), but markedly inhibited AM stemness. Of note, Nabhan et al. used Axin2-Cre-ERT2 mice for reporting Wnt signaling, as Axin2 is considered a conventional Wnt-β-catenin downstream gene (Nabhan et al., 2018). We found that a number of conventional Wnt-β-catenin downstream genes, including Myc and Axin2, were instead downregulated in AMs following Wnt treatment or IAV infection, suggesting that AM Wnt-β-catenin signaling probably differs from traditional β-catenin signaling in ATII cells. Further, even though our evidence suggested that Wnt production precedes AM β-catenin and HIF-1α

activation following IAV infection, HIF-1α activation has been shown to trigger conventional β-catenin-TCF signaling in stem cells under hypoxia (Mazumdar et al., 2010). Thus, future studies are warranted to address whether HIF-1α activation can feed back to AMs for stronger Wnt production and/or β-catenin activation following IAV infection *in vivo*.

Respiratory infection or injury often causes at least partial depletion of the resident AM pool at the peak of inflammation (Aegerter et al., 2020; Ghoneim et al., 2013; Hashimoto et al., 2013; Machiels et al., 2017; Misharin et al., 2017). Recruited monocytes can potentially give rise to a large proportion of the AM compartment, and monocyte-derived AMs can persist long-term following influenza, gammaherpesvirus infection, and bleomycin treatment (Aegerter et al., 2020; Machiels et al., 2017; Misharin et al., 2017). Conversely, evidence has also suggested that AM proliferation is the primary source of AM repopulation during influenza and adenovirus infection (Hashimoto et al., 2013; Jenkins et al., 2011; Yao et al., 2018). Consistent with this notion, our parabiosis and monocyte transfer experiments suggest that circulating monocytes are probably not a major contributor to AM repopulation at day 15 post-IAV infection. Thus, the relative contributions in terms of monocyte differentiation or macrophage local proliferation in AM pool regeneration following their partial depletion likely to depended on the context of injury and/or experimental models. Additionally, previous results (Hashimoto et al., 2013) and our studies here mainly focused on AM proliferation and repopulation at a relatively early time points (i.e., within 15 d.p.i.) immediately following AM partial depletion, while those studies revealing monocyte differentiation as a major contributor to AM regeneration were performed at much later time points (at least 4 weeks post-infection) (Aegerter et al., 2020; Machiels et al., 2017; Misharin et al., 2017). Thus, the extent of AM pool regeneration from either self-proliferation or monocyte differentiation may also depend on the timing of assessment given that recruited monocytes need a significant period of time to fully gain AM identity.

Our data suggest that there is a transition from proinflammatory macrophages to pro-repair macrophages in the AM compartment throughout the course of influenza infection. Strong β-catenin signaling promotes AM inflammatory activities at the peak of viral replication and pulmonary inflammation (i.e., 6 d.p.i.). Conversely, weak β-catenin signaling in AMs following viral clearance (i.e., 10–15 d.p.i.) facilitates their phenotypic transition to pro-repair function, helping to regenerate the damaged lung parenchyma. At the cellular level, there seems to be a selective expansion of AMs harboring high-reparative but low-inflammatory activities (β-catenin-HIF-1α^{low}) at the recovery stage. In parallel, AMs with high-inflammatory activities but low-healing functions (β-catenin-HIF-1α^{hi}) are prone to death (likely pyroptosis). The loss of β-catenin-HIF-1α^{hi} AMs in combination with the preferential expansion of β-catenin-HIF-1α^{low} AMs would certainly lead to the phenotypic transition of AMs *in vivo* over time. Of note, macrophages are also highly plastic when responding to local environmental changes. It thus remains possible that part of the wound-healing AM pool may derive directly from those β-catenin-HIF-1α^{hi} AMs following the disappearance of environmental Wnt. The relative contribution of selective expansion of HIF-1α^{low} cells versus direct switch from HIF-1α^{hi} cells in the AM phenotypic transition from proinflammatory to pro-repair function *in vivo* requires further investigation. Nevertheless, our data have highlighted potential roles of selective expansions of different macrophage populations in regulating the *in vivo* phenotypic and functional dynamics of macrophages during diseases.

Limitations of study

One limitation of our study is the current lack of an AM-specific Cre strain that would selectively delete floxed β-catenin or HIF-1α only from AMs. Even though we have provided multiple lines of evidence that strongly suggest the function of β-catenin and HIF-1α in AMs in regulating host morbidity and recovery, this study cannot completely exclude the possibility that β-catenin or HIF-1α deficiency in cells other than AMs might contribute to host diseases following IAV infection. Furthermore, beyond the correlative data we have provided on Wnt and HIF-1α expression during COVID-19 inflammation, future studies using SARS-CoV-2 animal models are needed to provide more definitive evidence on the roles of β-catenin and HIF-1α signaling in SARS-CoV-2 pathogenesis.

STAR★METHODS

Detailed methods are provided in the online version of this paper and include the following:

- KEY RESOURCES TABLE
- RESOURCE AVAILABILITY
  - Lead contact
  - Materials availability
  - Data and code availability
- EXPERIMENTAL MODEL AND SUBJECT DETAILS
- METHOD DETAILS
  - Mouse and infection
  - Broncho-alveolar lavage (BAL) fluid
  - Multiplex cytokine/chemokine quantification
  - ELISA analysis of BAL cytokines
  - BCA protein assay
  - Plaque assay
  - Mouse AM culture and treatment *in vitro*
  - Wnt3a treatment *in vivo*
  - Human AM culture and treatment *in vitro*
  - Quantitative RT-PCR
  - RT^2 profiler PCR array
  - Nanostring analysis
  - Colony formation assays
  - Parabiosis
  - Cell depletion
  - Immunofluorescence staining
  - Tamoxifen treatment
  - Lung histopathology
  - Co-immunoprecipitation
  - Western blot analysis
  - Metabolic analysis
  - Transmission electron microscopy
  - Bone marrow chimera
  - Single-cell RNA sequencing
  - RNA-seq
  - Chromatin immunoprecipitation (ChIP)
  - BrdU incorporation
  - Cell cycle analysis

- Lung and bone marrow cell suspension preparation
- Flow cytometry analysis
- Apoptosis analysis
- HIF-1α inhibitor treatment

● QUANTIFICATION AND STATISTICAL ANALYSIS

SUPPLEMENTAL INFORMATION

Supplemental information can be found online at https://doi.org/10.1016/j.immuni.2021.04.001.

ACKNOWLEDGMENTS

We thank the NIH Tetramer Core, the Mayo Flow Cytometry and Genomic cores, and Drs. M. Tanaka, K. Khanna, and A. Robling for assistance. This study was funded by NIH grants AI112844, AI147394, AG069264, and AG047156 and Mayo Clinic Kogod Aging Center and Center for Biomedical Discovery funds to J.S., as well as NIH grants AI129241 to M.H.K and AI067545 to A.W.G.

AUTHOR CONTRIBUTIONS

Conception, B.Z. and J.S.; data acquisition, B.Z., S.H., Y.W., R.Z., Y.M.S., C.L., I.S.C., X.G., M.W., and X.Z.; data analysis, B.Z., Y.W., S.H., Y.C., and J.S; manuscript writing, B.Z. and J.S.; reagents and manuscript editing, Q.N., A.T.P., S.B., M.M.T., M.M., V.S.S., H.Z., J.J.M., E.S.E., J.S.R., N.D., R.M.K., R.C., W.C., M.H.K., X.Z., and A.W.G.; funding acquisition, J.S.

DECLARATION OF INTERESTS

A.W.G. is a member of the advisory board of Pandion Therapeutics and ArsenalBio. The J.S. lab receives research grants from Evive Biotech and Humanigen.

Received: July 31, 2020
Revised: January 8, 2021
Accepted: March 31, 2021
Published: May 4, 2021

REFERENCES

Aegerter, H., Kulikauskaite, J., Crotta, S., Patel, H., Kelly, G., Hessel, E.M., Mack, M., Beinke, S., and Wack, A. (2020). Influenza-induced monocyte-derived alveolar macrophages confer prolonged antibacterial protection. Nat. Immunol. *21*, 145–157.

Caputa, G., Castoldi, A., and Pearce, E.J. (2019). Metabolic adaptations of tissue-resident immune cells. Nat. Immunol. *20*, 793–801.

Cardani, A., Boulton, A., Kim, T.S., and Braciale, T.J. (2017). Alveolar Macrophages Prevent Lethal Influenza Pneumonia By Inhibiting Infection Of Type-1 Alveolar Epithelial Cells. PLoS Pathog. *13*, e1006140.

Channappanavar, R., and Perlman, S. (2017). Pathogenic human coronavirus infections: causes and consequences of cytokine storm and immunopathology. Semin. Immunopathol. *39*, 529–539.

Channappanavar, R., Fehr, A.R., Vijay, R., Mack, M., Zhao, J., Meyerholz, D.K., and Perlman, S. (2016). Dysregulated Type I Interferon and Inflammatory Monocyte-Macrophage Responses Cause Lethal Pneumonia in SARS-CoV-Infected Mice. Cell Host Microbe *19*, 181–193.

Chapman, H.A., Li, X., Alexander, J.P., Brumwell, A., Lorizio, W., Tan, K., Sonnenberg, A., Wei, Y., and Vu, T.H. (2011). Integrin α6β4 identifies an adult distal lung epithelial population with regenerative potential in mice. J. Clin. Invest. *121*, 2855–2862.

Cheng, S.C., Quintin, J., Cramer, R.A., Shepardson, K.M., Saeed, S., Kumar, V., Giamarellos-Bourboulis, E.J., Martens, J.H., Rao, N.A., Aghajanirefah, A., et al. (2014). mTOR- and HIF-1α-mediated aerobic glycolysis as metabolic basis for trained immunity. Science *345*, 1250684.

Clevers, H., and Nusse, R. (2012). Wnt/β-catenin signaling and disease. Cell *149*, 1192–1205.

Cramer, T., Yamanishi, Y., Clausen, B.E., Förster, I., Pawlinski, R., Mackman, N., Haase, V.H., Jaenisch, R., Corr, M., Nizet, V., et al. (2003). HIF-1alpha is essential for myeloid cell-mediated inflammation. Cell *112*, 645–657.

del Peso, L., Castellanos, M.C., Temes, E., Martin-Puig, S., Cuevas, Y., Olmos, G., and Landazuri, M.O. (2003). The von Hippel Lindau/hypoxia-inducible factor (HIF) pathway regulates the transcription of the HIF-proline hydroxylase genes in response to low oxygen. J. Biol. Chem. *278*, 48690–48695.

Desai, T.J., Brownfield, D.G., and Krasnow, M.A. (2014). Alveolar progenitor and stem cells in lung development, renewal and cancer. Nature *507*, 190–194.

Desch, A.N., Gibbings, S.L., Goyal, R., Kolde, R., Bednarek, J., Bruno, T., Slansky, J.E., Jacobelli, J., Mason, R., Ito, Y., et al. (2016). Flow Cytometric Analysis of Mononuclear Phagocytes in Nondiseased Human Lung and Lung-Draining Lymph Nodes. Am. J. Respir. Crit. Care Med. *193*, 614–626.

Ghoneim, H.E., Thomas, P.G., and McCullers, J.A. (2013). Depletion of alveolar macrophages during influenza infection facilitates bacterial superinfections. J. Immunol. *191*, 1250–1259.

Gwyer Findlay, E., and Hussell, T. (2012). Macrophage-mediated inflammation and disease: a focus on the lung. Mediators Inflamm. *2012*, 140937.

Harada, N., Tamai, Y., Ishikawa, T., Sauer, B., Takaku, K., Oshima, M., and Taketo, M.M. (1999). Intestinal polyposis in mice with a dominant stable mutation of the beta-catenin gene. EMBO J. *18*, 5931–5942.

Hashimoto, D., Chow, A., Noizat, C., Teo, P., Beasley, M.B., Leboeuf, M., Becker, C.D., See, P., Price, J., Lucas, D., et al. (2013). Tissue-resident macrophages self-maintain locally throughout adult life with minimal contribution from circulating monocytes. Immunity *38*, 792–804.

Huang, S., Zhu, B., Cheon, I.S., Goplen, N.P., Jiang, L., Zhang, R., Peebles, R.S., Mack, M., Kaplan, M.H., Limper, A.H., and Sun, J. (2019). PPAR-γ in Macrophages Limits Pulmonary Inflammation and Promotes Host Recovery following Respiratory Viral Infection. J. Virol. *93*, e00030-19.

Huprikar, J., and Rabinowitz, S. (1980). A simplified plaque assay for influenza viruses in Madin-Darby kidney (MDCK) cells. J. Virol. Methods *1*, 117–120.

Hussell, T., and Bell, T.J. (2014). Alveolar macrophages: plasticity in a tissue-specific context. Nat. Rev. Immunol. *14*, 81–93.

Iwasaki, A., and Pillai, P.S. (2014). Innate immunity to influenza virus infection. Nat. Rev. Immunol. *14*, 315–328.

Izquierdo, H.M., Brandi, P., Gómez, M.J., Conde-Garrosa, R., Priego, E., Enamorado, M., Martínez-Cano, S., Sánchez, I., Conejero, L., Jimenez-Carretero, D., et al. (2018). Von Hippel-Lindau Protein Is Required for Optimal Alveolar Macrophage Terminal Differentiation, Self-Renewal, and Function. Cell Rep. *24*, 1738–1746.

Jenkins, S.J., Ruckerl, D., Cook, P.C., Jones, L.H., Finkelman, F.D., van Rooijen, N., MacDonald, A.S., and Allen, J.E. (2011). Local macrophage proliferation, rather than recruitment from the blood, is a signature of TH2 inflammation. Science *332*, 1284–1288.

Kaidi, A., Williams, A.C., and Paraskeva, C. (2007). Interaction between beta-catenin and HIF-1 promotes cellular adaptation to hypoxia. Nat. Cell Biol. *9*, 210–217.

Kamran, P., Sereti, K.I., Zhao, P., Ali, S.R., Weissman, I.L., and Ardehali, R. (2013). Parabiosis in mice: a detailed protocol. J. Vis. Exp. (80).

Klochendler, A., Weinberg-Corem, N., Moran, M., Swisa, A., Pochet, N., Savova, V., Vikeså, J., Van de Peer, Y., Brandeis, M., Regev, A., et al. (2012). A transgenic mouse marking live replicating cells reveals in vivo transcriptional program of proliferation. Dev. Cell *23*, 681–690.

Kumagai, Y., Takeuchi, O., Kato, H., Kumar, H., Matsui, K., Morii, E., Aozasa, K., Kawai, T., and Akira, S. (2007). Alveolar macrophages are the primary interferon-alpha producer in pulmonary infection with RNA viruses. Immunity *27*, 240–252.

Lee, K., Kang, J.E., Park, S.K., Jin, Y., Chung, K.S., Kim, H.M., Lee, K., Kang, M.R., Lee, M.K., Song, K.B., et al. (2010). LW6, a novel HIF-1 inhibitor, promotes proteasomal degradation of HIF-1alpha via upregulation of VHL in a colon cancer cell line. Biochem. Pharmacol. *80*, 982–989.

Lee, J.H., Tammela, T., Hofree, M., Choi, J., Marjanovic, N.D., Han, S., Canner, D., Wu, K., Paschini, M., Bhang, D.H., et al. (2017). Anatomically and Functionally Distinct Lung Mesenchymal Populations Marked by Lgr5 and Lgr6. Cell *170*, 1149–1163.e12.

Li, C., Zhu, B., Son, Y.M., Wang, Z., Jiang, L., Xiang, M., Ye, Z., Beckermann, K.E., Wu, Y., Jenkins, J.W., et al. (2019). The Transcription Factor Bhlhe40 Programs Mitochondrial Regulation of Resident $CD8^+$ T Cell Fitness and Functionality. Immunity *51*, 491–507.e7.

Liao, M., Liu, Y., Yuan, J., Wen, Y., Xu, G., Zhao, J., Cheng, L., Li, J., Wang, X., Wang, F., et al. (2020). Single-cell landscape of bronchoalveolar immune cells in patients with COVID-19. Nat. Med. *26*, 842–844.

Logan, C.Y., and Nusse, R. (2004). The Wnt signaling pathway in development and disease. Annu. Rev. Cell Dev. Biol. *20*, 781–810.

Londrigan, S.L., Short, K.R., Ma, J., Gillespie, L., Rockman, S.P., Brooks, A.G., and Reading, P.C. (2015). Infection of Mouse Macrophages by Seasonal Influenza Viruses Can Be Restricted at the Level of Virus Entry and at a Late Stage in the Virus Life Cycle. J. Virol. *89*, 12319–12329.

Machiels, B., Dourcy, M., Xiao, X., Javaux, J., Mesnil, C., Sabatel, C., Desmecht, D., Lallemand, F., Martinive, P., Hammad, H., et al. (2017). A gammaherpesvirus provides protection against allergic asthma by inducing the replacement of resident alveolar macrophages with regulatory monocytes. Nat. Immunol. *18*, 1310–1320.

Macosko, E.Z., Basu, A., Satija, R., Nemesh, J., Shekhar, K., Goldman, M., Tirosh, I., Bialas, A.R., Kamitaki, N., Martersteck, E.M., et al. (2015). Highly Parallel Genome-wide Expression Profiling of Individual Cells Using Nanoliter Droplets. Cell *161*, 1202–1214.

Manicassamy, S., Reizis, B., Ravindran, R., Nakaya, H., Salazar-Gonzalez, R.M., Wang, Y.C., and Pulendran, B. (2010). Activation of beta-catenin in dendritic cells regulates immunity versus tolerance in the intestine. Science *329*, 849–853.

Manoharan, I., Hong, Y., Suryawanshi, A., Angus-Hill, M.L., Sun, Z., Mellor, A.L., Munn, D.H., and Manicassamy, S. (2014). TLR2-dependent activation of β-catenin pathway in dendritic cells induces regulatory responses and attenuates autoimmune inflammation. J. Immunol. *193*, 4203–4213.

Mazumdar, J., O'Brien, W.T., Johnson, R.S., LaManna, J.C., Chavez, J.C., Klein, P.S., and Simon, M.C. (2010). O2 regulates stem cells through Wnt/β-catenin signalling. Nat. Cell Biol. *12*, 1007–1013.

Mei, J., Riedel, N., Grittner, U., Endres, M., Banneke, S., and Emmrich, J.V. (2018). Body temperature measurement in mice during acute illness: implantable temperature transponder versus surface infrared thermometry. Sci. Rep. *8*, 3526.

Merad, M., and Martin, J.C. (2020). Pathological inflammation in patients with COVID-19: a key role for monocytes and macrophages. Nat. Rev. Immunol. *20*, 355–362.

Minutti, C.M., Knipper, J.A., Allen, J.E., and Zaiss, D.M. (2017). Tissue-specific contribution of macrophages to wound healing. Semin. Cell Dev. Biol. *61*, 3–11.

Misharin, A.V., Morales-Nebreda, L., Reyfman, P.A., Cuda, C.M., Walter, J.M., McQuattie-Pimentel, A.C., Chen, C.I., Anekalla, K.R., Joshi, N., Williams, K.J.N., et al. (2017). Monocyte-derived alveolar macrophages drive lung fibrosis and persist in the lung over the life span. J. Exp. Med. *214*, 2387–2404.

Miyake, Y., Asano, K., Kaise, H., Uemura, M., Nakayama, M., and Tanaka, M. (2007). Critical role of macrophages in the marginal zone in the suppression of immune responses to apoptotic cell-associated antigens. J. Clin. Invest. *117*, 2268–2278.

Morris, S.L., and Huang, S. (2016). Crosstalk of the Wnt/β-catenin pathway with other pathways in cancer cells. Genes Dis. *3*, 41–47.

Nabhan, A.N., Brownfield, D.G., Harbury, P.B., Krasnow, M.A., and Desai, T.J. (2018). Single-cell Wnt signaling niches maintain stemness of alveolar type 2 cells. Science *359*, 1118–1123.

Newton, A.H., Cardani, A., and Braciale, T.J. (2016). The host immune response in respiratory virus infection: balancing virus clearance and immunopathology. Semin. Immunopathol. *38*, 471–482.

Pernet, E., Downey, J., Vinh, D.C., Powell, W.S., and Divangahi, M. (2019). Leukotriene B_4-type I interferon axis regulates macrophage-mediated disease tolerance to influenza infection. Nat. Microbiol. *4*, 1389–1400.

Purnama, C., Ng, S.L., Tetlak, P., Setiagani, Y.A., Kandasamy, M., Baalasubramanian, S., Karjalainen, K., and Ruedl, C. (2014). Transient ablation of alveolar macrophages leads to massive pathology of influenza infection without affecting cellular adaptive immunity. Eur. J. Immunol. *44*, 2003–2012.

Rajagopal, J., Carroll, T.J., Guseh, J.S., Bores, S.A., Blank, L.J., Anderson, W.J., Yu, J., Zhou, Q., McMahon, A.P., and Melton, D.A. (2008). Wnt7b stimulates embryonic lung growth by coordinately increasing the replication of epithelium and mesenchyme. Development *135*, 1625–1634.

Reya, T., Duncan, A.W., Ailles, L., Domen, J., Scherer, D.C., Willert, K., Hintz, L., Nusse, R., and Weissman, I.L. (2003). A role for Wnt signalling in self-renewal of haematopoietic stem cells. Nature *423*, 409–414.

Rubins, J.B. (2003). Alveolar macrophages: wielding the double-edged sword of inflammation. Am. J. Respir. Crit. Care Med. *167*, 103–104.

Satija, R., Farrell, J.A., Gennert, D., Schier, A.F., and Regev, A. (2015). Spatial reconstruction of single-cell gene expression data. Nat. Biotechnol. *33*, 495–502.

Schneider, C., Nobs, S.P., Heer, A.K., Kurrer, M., Klinke, G., van Rooijen, N., Vogel, J., and Kopf, M. (2014). Alveolar macrophages are essential for protection from respiratory failure and associated morbidity following influenza virus infection. PLoS Pathog. *10*, e1004053.

Short, K.R., Kroeze, E.J.B.V., Fouchier, R.A.M., and Kuiken, T. (2014). Pathogenesis of influenza-induced acute respiratory distress syndrome. Lancet Infect. Dis. *14*, 57–69.

Sieweke, M.H., and Allen, J.E. (2013). Beyond stem cells: self-renewal of differentiated macrophages. Science *342*, 1242974.

Sohn, Y.S., Tamir, S., Song, L., Michaeli, D., Matouk, I., Conlan, A.R., Harir, Y., Holt, S.H., Shulaev, V., Paddock, M.L., et al. (2013). NAF-1 and mitoNEET are central to human breast cancer proliferation by maintaining mitochondrial homeostasis and promoting tumor growth. Proc. Natl. Acad. Sci. USA *110*, 14676–14681.

Soucie, E.L., Weng, Z., Geirsdóttir, L., Molawi, K., Maurizio, J., Fenouil, R., Mossadegh-Keller, N., Gimenez, G., VanHille, L., Beniazza, M., et al. (2016). Lineage-specific enhancers activate self-renewal genes in macrophages and embryonic stem cells. Science *351*, aad5510.

Stuart, T., Butler, A., Hoffman, P., Hafemeister, C., Papalexi, E., Mauck, W.M., 3rd, Hao, Y., Stoeckius, M., Smibert, P., and Satija, R. (2019). Comprehensive Integration of Single-Cell Data. Cell *177*, 1888–1902.e1821.

Subramanian, A., Tamayo, P., Mootha, V.K., Mukherjee, S., Ebert, B.L., Gillette, M.A., Paulovich, A., Pomeroy, S.L., Golub, T.R., Lander, E.S., and Mesirov, J.P. (2005). Gene set enrichment analysis: a knowledge-based approach for interpreting genome-wide expression profiles. Proc. Natl. Acad. Sci. USA *102*, 15545–15550.

Sun, J., Dodd, H., Moser, E.K., Sharma, R., and Braciale, T.J. (2011). CD4+ T cell help and innate-derived IL-27 induce Blimp-1-dependent IL-10 production by antiviral CTLs. Nat. Immunol. *12*, 327–334.

Sun, J., Madan, R., Karp, C.L., and Braciale, T.J. (2009). Effector T cells control lung inflammation during acute influenza virus infection by producing IL-10. Nat. Med. *15*, 277–284.

Suryawanshi, A., Tadagavadi, R.K., Swafford, D., and Manicassamy, S. (2016). Modulation of Inflammatory Responses by Wnt/β-Catenin Signaling in Dendritic Cells: A Novel Immunotherapy Target for Autoimmunity and Cancer. Front. Immunol. *7*, 460.

Tannahill, G.M., Curtis, A.M., Adamik, J., Palsson-McDermott, E.M., McGettrick, A.F., Goel, G., Frezza, C., Bernard, N.J., Kelly, B., Foley, N.H., et al. (2013). Succinate is an inflammatory signal that induces IL-1β through HIF-1α. Nature *496*, 238–242.

Tate, M.D., Pickett, D.L., van Rooijen, N., Brooks, A.G., and Reading, P.C. (2010). Critical role of airway macrophages in modulating disease severity during influenza virus infection of mice. J. Virol. *84*, 7569–7580.

Tay, M.Z., Poh, C.M., Rénia, L., MacAry, P.A., and Ng, L.F.P. (2020). The trinity of COVID-19: immunity, inflammation and intervention. Nat. Rev. Immunol. *20*, 363–374.

Tirosh, I., Izar, B., Prakadan, S.M., Wadsworth, M.H., 2nd, Treacy, D., Trombetta, J.J., Rotem, A., Rodman, C., Lian, C., Murphy, G., et al. (2016). Dissecting the multicellular ecosystem of metastatic melanoma by single-cell RNA-seq. Science *352*, 189–196.

Trapnell, C., Williams, B.A., Pertea, G., Mortazavi, A., Kwan, G., van Baren, M.J., Salzberg, S.L., Wold, B.J., and Pachter, L. (2010). Transcript assembly and quantification by RNA-Seq reveals unannotated transcripts and isoform switching during cell differentiation. Nat. Biotechnol. *28*, 511–515.

Ural, B.B., Yeung, S.T., Damani-Yokota, P., Devlin, J.C., de Vries, M., Vera-Licona, P., Samji, T., Sawai, C.M., Jang, G., Perez, O.A., et al. (2020). Identification of a nerve-associated, lung-resident interstitial macrophage subset with distinct localization and immunoregulatory properties. Sci. Immunol. *5*, eaax8756.

Wang, J., Nikrad, M.P., Phang, T., Gao, B., Alford, T., Ito, Y., Edeen, K., Travanty, E.A., Kosmider, B., Hartshorn, K., and Mason, R.J. (2011). Innate immune response to influenza A virus in differentiated human alveolar type II cells. Am. J. Respir. Cell Mol. Biol. *45*, 582–591.

Wang, Z., Wang, S., Goplen, N.P., Li, C., Cheon, I.S., Dai, Q., Huang, S., Shan, J., Ma, C., Ye, Z., et al. (2019). PD-1(hi) CD8(+) resident memory T cells balance immunity and fibrotic sequelae. Sci. Immunol. *4*, eaaw1217.

Wellenstein, M.D., Coffelt, S.B., Duits, D.E.M., van Miltenburg, M.H., Slagter, M., de Rink, I., Henneman, L., Kas, S.M., Prekovic, S., Hau, C.S., et al. (2019). Loss of p53 triggers WNT-dependent systemic inflammation to drive breast cancer metastasis. Nature *572*, 538–542.

Wong, D.J., Liu, H., Ridky, T.W., Cassarino, D., Segal, E., and Chang, H.Y. (2008). Module map of stem cell genes guides creation of epithelial cancer stem cells. Cell Stem Cell *2*, 333–344.

Xi, Y., Kim, T., Brumwell, A.N., Driver, I.H., Wei, Y., Tan, V., Jackson, J.R., Xu, J., Lee, D.K., Gotts, J.E., et al. (2017). Local lung hypoxia determines epithelial fate decisions during alveolar regeneration. Nat. Cell Biol. *19*, 904–914.

Yao, S., Buzo, B.F., Pham, D., Jiang, L., Taparowsky, E.J., Kaplan, M.H., and Sun, J. (2013). Interferon regulatory factor 4 sustains CD8(+) T cell expansion and effector differentiation. Immunity *39*, 833–845.

Yao, Y., Jeyanathan, M., Haddadi, S., Barra, N.G., Vaseghi-Shanjani, M., Damjanovic, D., Lai, R., Afkhami, S., Chen, Y., Dvorkin-Gheva, A., et al. (2018). Induction of Autonomous Memory Alveolar Macrophages Requires T Cell Help and Is Critical to Trained Immunity. Cell *175*, 1634–1650.e1617.

Zhang, L., and Liu, Y. (2020). Potential interventions for novel coronavirus in China: A systematic review. J. Med. Virol. *92*, 479–490.

Zhu, B., Zhang, R., Li, C., Jiang, L., Xiang, M., Ye, Z., Kita, H., Melnick, A.M., Dent, A.L., and Sun, J. (2019). BCL6 modulates tissue neutrophil survival and exacerbates pulmonary inflammation following influenza virus infection. Proc. Natl. Acad. Sci. USA *116*, 11888–11893.

STAR★METHODS

KEY RESOURCES TABLE

REAGENT or RESOURCE	SOURCE	IDENTIFIER
Antibodies		
Anti Non-phospho (Active) β-catenin (clone D13A1)	Cell Signaling Technology	Cat# 8814; RRID: AB_2798251
Anti β-catenin (clone D10A8)	Cell Signaling Technology	Cat# 8480; RRID: AB_11127855
Anti HIF-1α (clone D2U3T)	Cell Signaling Technology	Cat# 14179; RRID: AB_2622225
Anti TCF4 (clone C9B9)	Cell Signaling Technology	Cat# 2565; RRID: AB_2561041
Anti β-actin (clone C4)	Santa Cruz Biotechnology	Cat# sc-47778; RRID: AB_2714189
Anti SiglecF-BV421 (clone E50-2440)	BD Biosciences	Cat# 562681; RRID: AB_2722581
Anti SiglecF-PE (clone E50-2440)	BD Biosciences	Cat# 552126; RRID: AB_394341
Anti CD11b-PerCP-Cy5.5 (clone M1/70)	Biolegend	Cat# 101228; RRID: AB_893232
Anti CD11c-BV510 (clone N418)	Biolegend	Cat# 117338; RRID: AB_2562016
Anti MHCII-FITC (clone M5/114.15.2)	Biolegend	Cat# 107606; RRID: AB_313321
Anti Ly6G-PE-Cy7 (clone 1A8)	Biolegend	Cat# 127618; RRID: AB_1877261
Anti Ly6C-BV711 (clone HK1.4)	Biolegend	Cat# 128037; RRID: AB_2562630
Anti CD64-BV711 (clone X54-5/7.1)	Biolegend	Cat# 139311; RRID: AB_2563846
Anti CD64-PE (clone X54-5/7.1)	Biolegend	Cat# 139304; RRID: AB_10612740
Anti MerTK- APC (clone 2B10C42)	Biolegend	Cat# 151508; RRID: AB_2650739
Anti MerTK- FITC (clone 2B10C42)	Biolegend	Cat# 151504; RRID: AB_2617035
Anti CX3CR1-BV605 (clone SA011F11)	Biolegend	Cat# 149027; RRID: AB_2565937
Anti CD169-APC (clone 3D6.112)	Biolegend	Cat# 142418; RRID: AB_2565641
Anti CD206-APC (clone C068C2)	Biolegend	Cat# 141708; RRID: AB_10900231
Anti CD4-BV510 (clone RM4-5)	Biolegend	Cat# 100559; RRID: AB_2562608
Anti CD8-PerCP-Cy5.5(clone YTS156.7.7)	Biolegend	Cat# 126610; RRID: AB_2260149
Anti human HLA-DR-PerCP-Cy5.5 (clone L243)	Biolegend	Cat# 307630; RRID: AB_893567
Anti human CD64-BV421 (clone 10.1)	Biolegend	Cat# 305019; RRID: AB_2561538
Anti CD45-APC-Cy7 (clone 30-F11)	Biolegend	Cat# 103116; RRID: AB_312981
Anti CD45.1-BV421 (clone A20)	Biolegend	Cat# 110732; RRID: AB_2562563
Anti CD45.2- PerCP-Cy5.5 (clone 104)	Tonbo Biosciences	Cat# 65-0454-U100; RRID: AB_2621894
Anti Ki67-FITC (clone SolA15)	eBioscience	Cat# 11-5698-82; RRID: AB_11151330
Anti Ki67-APC (clone SolA15)	eBioscience	Cat# 17-5698-82; RRID: AB_2688057
Anti HIF-1α-PE (clone 241812)	R&D Systems	Cat# IC1935P; RRID: AB_2232941
Anti HIF-1α-APC (clone 241812)	R&D Systems	Cat# IC1935A; RRID: AB_1061580
Anti β-catenin-PE (clone D10A8)	Cell Signaling Technology	Cat# 14903; RRID: AB_2798642
Anti Non-phospho (Active) β-catenin-PE (clone D13A1)	Cell Signaling Technology	Cat# 13537; RRID: AB_2798251
Anti Non-phospho (Active) β-catenin-FTIC (clone D2U8Y)	Cell Signaling Technology	Cat# 70034; RRID: AB_2799770
Anti Mouse IgG, HRP Conjugate	Promega	Cat# W4028; RRID: AB_430834
Anti Rabbit IgG, HRP Conjugate	Promega	Cat# W4018; RRID: AB_430833
Influenza NP_{366} Tetramer	NIH Tetramer Facility	Cat# H-2D(b) ASNENMETM
Influenza PA_{224} Tetramer	NIH Tetramer Facility	Cat# H-2D(b) SSLENFRAYV
Bacterial and virus strains		
Influenza A/PR8/34	Laboratory of Thomas Braciale	Sun et al., 2011

(*Continued on next page*)

Continued

REAGENT or RESOURCE	SOURCE	IDENTIFIER
Biological samples		
Broncho-alveolar lavage Fluid from adult donors	Mayo Clinic	https://www.mayoclinic.org/
Chemicals, peptides, and recombinant proteins		
Diphtheria Toxin	Sigma-Aldrich	Cat# D0564
Tamoxifen	Sigma-Aldrich	Cat# T5648
7-AAD Viability Staining Solution	Biolegend	Cat# 420403
MethoCult Methylcellulose-based medium	STEMCELL Technologies	Cat# 03231
Seahorse XF Media & Calibrant	Agilent	Cat# 102353-100
Glucose D(+)	Sigma-Aldrich	Cat# 50-99-7
Oligomycin	Sigma-Aldrich	Cat # 1404-19-9
carbonyl cyanide-4-(trifluoromethoxy) phenylhydrazone	Sigma-Aldrich	Cat# 370-86-5
Rotenone	Sigma-Aldrich	Cat# 83-79-4
Antimycin A	Sigma-Aldrich	Cat# A8674
2-Deoxy-D-glucose	Sigma-Aldrich	Cat# 154-17-6
3-Nitropropionic Acid	Cayman Chemical	Cat# 504-88-1
LW6	TargetMol	Cat# T3494
Zombie NIR Fixable Viability Dye	Biolegend	Cat# 423106
Recombinant mouse Wnt3a protein	PeproTech	Cat# 315-20
Recombinant mouse GM-CSF	Biolegend	Cat# 576308
Recombinant human Wnt3a protein	Prospec-Tany Technogene	Cat# CYT-861
Recombinant Human GM-CSF (carrier-free)	Biolegend	Cat# 572903
Recombinant Human M-CSF (carrier-free)	Biolegend	Cat# 574804
Critical commercial assays		
GenElute Mammalian Total RNA Miniprep Kit	Sigma-Aldrich	Cat# RTN350
RNeasy Mini Kit	QIAGEN	Cat# 74104
RT^2 First Strand Kit	QIAGEN	Cat# 330404
RT^2 Profiler Mouse Wound Healing PCR Array	QIAGEN	Cat# PAMM-121Z
RT^2 Profiler Mouse WNT Signaling Pathway PCR Array	QIAGEN	Cat# PAMM-043Z
RT^2 Profiler Mouse Inflammatory Response & Autoimmunity PCR Array	QIAGEN	Cat# PAMM-077Z
FLICA 660 Caspase-1 Assay	ImmunoChemistry Technologies	Cat# 9122
Pacific Blue Annexin V Apoptosis Detection Kit	Biolegend	Cat# 640926
Propidium Iodide Flow Cytometry Kit	abcam	Cat# ab139418
BD PharMingen BrdU Flow Kits	BD Biosciences	Cat# 552598
eBioscience Foxp3 / Transcription Factor Staining Buffer Set	Thermo Fisher Scientific	Cat# 00-5523-00
Lung Dissociation Kit, mouse	Miltenyibiotec	Cat# 130-095-927
Seahorse XFp FluxPak	Agilent	Cat# 103022-100
Mouse Cytokine/Chemokine Magnetic Bead Panel	Luminex Cooperation	Cat# MCYTMAG-70K-PX32
ELISA MAX™ Standard Sets for Mouse CCL2	Biolegend	Cat# 432701
ELISA MAX™ Deluxe Sets for Mouse TNF-α	Biolegend	Cat# 430904
ELISA MAX™ Deluxe Sets for Mouse IL-1β	Biolegend	Cat# 432604

(*Continued on next page*)

Continued		
REAGENT or RESOURCE	SOURCE	IDENTIFIER
ELISA MAX Deluxe Sets for Mouse IL-6	Biolegend	Cat# 431304
Pierce BCA Protein Assay Kit	Thermo Fisher Scientific	Cat# 23225
nCounter Mouse Immunology Panel	NanoString Technologies	Cat# XT-CSO-MIM1-12
Deposited data		
Raw and analyzed data	This paper	GEO: GSE164793
RNA-seq of lung resident macrophages from naive mice	Ural et al., 2020	GEO: GSE146681
RNA-seq of human AMs infected with IAV	Wang et al., 2011	GEO: GSE30723
Single-cell landscape of bronchoalveolar immune cells in COVID-19 patients	Liao et al., 2020	GEO: GSE145926
Experimental models: Cell lines		
N/A	N/A	N/A
Experimental models: Organisms/strains		
C57BL/6J	The Jackson Laboratory	Cat# 000664
Ctnnb1$^{fl/fl}$	The Jackson Laboratory	Cat# 004152
CD11c-cre (Itgax-cre)	The Jackson Laboratory	Cat# 8068
Lyz2-cre	The Jackson Laboratory	Cat# 004781
CycB1-GFP	The Jackson Laboratory	Cat# 023345
ROSA^{mTmG}	The Jackson Laboratory	Cat# 007676
CD45.1	The Jackson Laboratory	Cat# 002014
Ccr2$^{-/-}$	The Jackson Laboratory	Cat# 004999
Ubc-cre ERT2	The Jackson Laboratory	Cat# 007001
Hif1a$^{fl/fl}$	The Jackson Laboratory	Cat#007561
CD169-DTR	Riken Bioresource	Miyake et al., 2007
Ctnnb1$_{exon3}^{fl/fl}$	Laboratory of Makoto Taketo	Harada et al., 1999
Egln3-YFP	Laboratory of Dr. Goldrath	This paper
SPC-cre ERT2	Laboratory of Hal Chapman	Chapman et al., 2011
Oligonucleotides		
Primers for mRNA expression, see Table S1	This paper	N/A
Primers for ChIP-qPCR, see Table S1	This paper	N/A
Recombinant DNA		
N/A	N/A	N/A
Software and algorithms		
GraphPad Prism 6	GraphPad Software	http://www.graphpad.com
FlowJo (version 10.3)	LLC	https://www.flowjo.com/
MeV software (version 4.9)	Dana-Farber Cancer Institute	http://mev.tm4.org
ImageJ	NIH software	https://imagej.nih.gov/ij/
nSolver 3.0	NanoString Technologies	https://www.nanostring.com/
Cell Ranger	10X Genomics	https://support.10xgenomics.com
Seurat	Satija et al., 2015	https://satijalab.org/seurat/
R language	The R Foundation	https://www.r-project.org/
GSEA	Broad Institute	http://software.broadinstitute.org/

RESOURCE AVAILABILITY

Lead contact

Further information and requests for resources and reagents should be directed to and will be fulfilled by the Lead Contact, Jie Sun (sun.jie@mayo.edu)

Materials availability

This study did not generate new unique reagents.

Data and code availability

The accession number for the bulk RNA-seq and scRNA-seq datasets reported in this paper is GEO: GSE164793.

EXPERIMENTAL MODEL AND SUBJECT DETAILS

All animal experiments were performed in animal housing facilities at the Indiana University School of Medicine (IUSM, Indianapolis, IN) or the Mayo Clinic (Rochester, MN). Sex- and age-matched 9-12 weeks old mice of both sexes were used in the experiments. All animal experiments were approved by the IUSM or the Mayo Clinic Institutional Animal Care and Use Committees (IACUC).

METHOD DETAILS

Mouse and infection

WT C57BL/6, CycB1-GFP, Lyz2-cre, CD11c-cre, *Ctnnb1*$^{fl/fl}$, *Hif1a*$^{fl/fl}$, *Ccr2*$^{-/-}$ and CD45.1^{+} congenic mice were purchased from the Jackson Laboratory and bred in house. *Ctnnb1*$_{exon3}$ $^{fl/fl}$ mice were obtained from Dr. Makoto Taketo (Kyoto University). *Egln3*-YFP mice were obtained from Dr. Ananda Goldrath (UCSD). *Ctnnb1*$^{\Delta Lyz2}$, or *Ctnnb1*$_{exon3}$$^{\Delta Lyz2}$ mice were generated by crossing *Ctnnb1*$^{fl/fl}$, or *Ctnnb1*$_{exon3}$ $^{fl/fl}$ mice with Lyz2-cre mice respectively. *Ctnnb1*$^{\Delta CD11c}$ or *Hif1a*$^{\Delta CD11c}$ were generated by crossing *Ctnnb1*$^{fl/fl}$ or *Hif1a*$^{fl/fl}$ mice with CD11c-cre mice respectively. *Ctnnb1*$^{\Delta Lyz2}$-CD169-DTR mice were generated by crossing *Ctnnb1*$^{\Delta Lyz2}$ mice with CD169-DTR mice. Control mice were Cre or CD169-DTR transgene negative littermates. *Ctnnb1*$^{\Delta SPC\text{-}cre\ ERT2}$ mice were generated by crossing *Ctnnb1*$^{fl/fl}$ mice to mice harboring Cre-ERT2-rtTA knock-in at Surfactant Protein C (SPC) locus (SPC-Cre ERT2) (Chapman et al., 2011). SPC-CreERT2/mTmG mice were created by crossing SPC-Cre ERT2 mice with a membrane-localized fluorescence reporter (ROSA^{mTmG}). All mice housed in a specific pathogen-free environment. For host morbidity experiments following regular dose of IAV infection, influenza A/PR8/34 virus strain (~200 PFU/mouse, sublethal) was diluted in FBS-free DMEM media (Corning) on ice and inoculated in anesthetized mice through intranasal route as described before (Sun et al., 2009). For host mortality experiments following high dose (2.5 folds of the sublethal dose) of IAV infection, the outcome was determined based on the humane endpoint (more than 30% weight loss or moribund) or deaths before humane sacrifice. Mouse body surface temperature profiles was monitered daily by non-contact infrared thermometer. During temperature acquisition, the tail was gently fixed and lifted while the animal gripped a metal rod on the cage lid, allowing the exposure of the perianal region, and the measurement was taken with the thermometer held 1-2 cm from the reading site (Mei et al., 2018). For all IAV infection experiments *in vivo*, WT littlemates without Cre transgene were used for transgenic mouse controls.

Broncho-alveolar lavage (BAL) fluid

BAL fluid was obtained by flushing the airway three times with a single inoculum of 600 μL sterile PBS via a trachea incision. Cells in BAL fluid were spun down and supernatants were collected for the determination of cytokines/chemokines levels, protein concentration and viral titers.

Multiplex cytokine/chemokine quantification

Cytokine and chemokine levels in BAL fluid were measured using a 32-plex-cytokine array according to the manufacturer's protocol (MCYTMAG-70K-PX32, EMD Millipore). 25 μl diluted BAL fluid sample was used in the assays. The result was read with Luminex instrument and analyzed with Milliplex software (Millipore).

ELISA analysis of BAL cytokines

50 μl of each BAL sample was analyzed with the ELISA using commercially available kits for mouse IL-1β, TNF-α, IL-6, and CCL2 (Biolegend) following the manufacturer's protocol. The VERSAmax microplate reader (Molecular Devices) was used for colorimetric quantification and analysis at 450 nm wavelength.

BCA protein assay

BCA protein assay kit was obtained from Thermo Scientific. 2 μl of each BAL sample was used. VERSAmax microplate reader (Molecular Devices) was used for colorimetric quantification and analysis at 570nm wavelength.

Plaque assay

IAV plaque assays were performed as described before (Huprikar and Rabinowitz, 1980). Briefly, MDCK cells were grown in 6-well plates and incubated with series dilution of BAL sample for 1 h. The plates were then overlaid with low melting temperature agarose (0.6%) in MEM with BSA and trypsin and cultured for 3 days in 37°C incubator. Plates were then fixed with formaldehyde and virus plaques were visualized with the staining of neutral red.

Mouse AM culture and treatment *in vitro*

Mouse AMs were obtained from BAL as described previously (Huang et al., 2019). Briefly, alveolar lavages were pooled from BAL washes (PBS with 2 mM EDTA). AMs were purified by adherence for 2 h in complete medium (RPMI-1640, 10% FBS, 1% Pen/Strep/glutamate) at 37 C and 5% CO_2. The non-adherent cells were washed off with warm PBS. The remaining adherent cells were cultured in complete medium supplemented with 10 ng/ml recombinant murine granulocyte macrophage CSF (GM-CSF).

For AM infection *in vitro*, seeded cells were infected with or without 10 MOI of influenza PR8 virus for 1 hour and then cultured in complete medium containing 10 ng/ml GM-CSF for overnight. For *ex vivo* AM culture, AMs were obtained from IAV-infected mice and cultured in complete medium for overnight. The cells were then washed and cultured with complete medium with 10 ng/ml GM-CSF for another overnight.

For AM treatment *in vitro*, AM were pre-treated with Wnt3a (100 ng/ml, unless specific indication), 2-DG (200 μM), Rotenone (100 nM), 3-NP (100 μM), Antimycin (200 nM) or vehicle in complete medium without GM-CSF for overnight. Subsequently, cells were washed with warm PBS and treated with the same amount of above reagents in complete medium with 10 ng/ml GM-CSF for another overnight. For hypoxic exposure, AM were placed in a hypoxia incubator (Eppendorf, USA) at 0.5% O_2.

Cells were analyzed by quantitative RT-PCR, western blot, ELISA or Flow cytometry.

Wnt3a treatment *in vivo*

C57BL/6 WT mice were injected with PBS or 3 μg Wnt3a through intranasal route at day 1 and day 2. Then, the BAL cells were collected for subsequent analysis at day 3.

Human AM culture and treatment *in vitro*

Human AMs ($HLADR^+CD64^+CD11c^+$) (Desch et al., 2016) were obtained from BAL fluid from adult patients undergo flexible bronchoscopy. AMs were purified by adherence for 2 h in complete medium (RPMI-1640, 10% FBS, 1% Pen/Strep/glutamate) at 37°C and 5% CO_2. The non-adherent cells were washed off with warm PBS. The remaining adherent cells were cultured in complete medium. For AM treatment *in vitro*, AMs were pre-treated with recombinant human Wnt3a (100 ng/ml), Wnt3a (100 ng/ml) plus LW6 (10 μM), or vehicle in complete medium for overnight. Subsequently, cells were washed with warm PBS and treated with the same amount of above reagents in complete medium supplemented with 50 ng/ml of recombinant human GM-CSF and M-CSF for another overnight. Cells were analyzed by quantitative RT-PCR or Flow cytometry.

We selected donors without a history of immunosuppression and chemo or radiotherapies, and are free of inflammation or pulmonary infection. The study involving human participants was reviewed and approved by the Institutional Review Board (IRB# 19-012187) at Mayo Clinic. All participants provided written informed consent prior to sample collection and subsequent analysis.

Quantitative RT-PCR

mRNA from cultured AMs, *in vivo* sorted AMs or homogenates from individual lungs as indicated in the text was isolated with Total RNA purification kit (Sigma) and treated with DNase I (Invitrogen). Random primers (Invitrogen) and Moloney murine leukemia virus (MMLV) reverse transcriptase (Invitrogen) were used to synthesize first-strand cDNAs from equivalent amounts of RNA from each sample. RT-PCR was performed with Fast SYBR Green PCR Master Mix (Applied Biosystems). RT-PCR was conducted in duplicates in QuantStudio3 (Applied Bioscience). Data were generated with the comparative threshold cycle (Delta CT) method by normalizing to hypoxanthine phosphoribosyltransferase (HPRT). Sequences of primers used in the studies are provided in the Table S1.

RT^2 profiler PCR array

Total RNA from lung tissue or AMs were extracted as described above. Equal amount of total RNA was used for the synthesis of first strand cDNA with kit from QIAGEN. First strand cDNA was mixed with 2xFast SYBR Green Master Mix (Applied Bioscience) and water in a formula directed in the manual. 25 μl of the mixture was added into each well of the 96 well plate provided by manufacture. The wells in the plate include different primers in each well to detect 84 target genes, housekeeping genes, negative and positive control genes. RT-PCR was conducted in QuantStudio3 (Applied Bioscience). Obtained raw data was analyzed in software provided by QIAGEN (accessible online on the website of QIAGEN). Beriefly, uploading the raw data, designating control group, selecting housekeeping gene to normalize results, and calculating the relative expression level were performed step-by-step according to the manufacturer's instructions.

Nanostring analysis

Total RNA from sorted AMs or monocytes was extracted with mini RNA Kit (QIAGEN). Equal amount of total RNA from different cells was used for a murine immunology panel (Nanosting Technologies) (Wang et al., 2019). Hybridization reaction was established by following the instruction of manufacture. Aliquots of Reporter Codeset and Capture probeset were thawed at room temperature. Then a master mix was created by adding 70 μl of hybridization buffer to the tube containing the reporter codeset. 8 μl of this master mix was added to each of tubes for different samples, 5 μl (50 ng) of total RNA sample was added into each tube. Then 2 μl of well mixed Capture probeset was added to each tube and placed in the preheated 65°C thermal cycler. All the sample mixes were incubated for 16 hours at 65°C for completion of hybridization. The samples were then loaded into the sample hole in the cartridge and loaded into the NanoString nCounter SPRINT Profiler machine (NanoString). When corresponding RLF running is finished, the raw data was downloaded and analyzed with Nanostring software nSolver 3.0 (Nanostring). mRNA counts were processed to account

for hybridization efficiency, background noise, and sample content, and were normalized using the geometric mean of housekeeping genes. Fold changes were calculated by comparing the experimental group to the appropriate controls. Transcript counts less than the mean of the negative control transcripts for each sample were considered as background.

Colony formation assays

Colony formation assays were performed as described (Soucie et al., 2016). Briefly, freshly isolated AMs were seeded at 20,000 cells in 35 mm culture dishes, and pre-treated with or without Wnt3a (100 ng/ml) for overnight at 37°C, 5% CO_2. The cells were then washed with PBS followed by the addition of MethoCult medium (M3231, Stem Cell Technologies) supplemented with 10 ng/ml GM-CSF, 50 μg/ml penicillin/streptomycin and 2 mM glutamine in the presence or absence of wnt3a (100 ng/ml). The number of colonies were counted on day 18 after plating. Where indicated, rotenone (100 nM), 3-NP (100 μM) or Antimycin (200 nM) were added as described for Wnt3a.

Parabiosis

Age- and weight- matched female C57BL/6 congenic CD45.2 and CD45.1 mice or *Ctnnb1*$^{fl/fl}$ and *Ctnnb1*$^{\Delta Lyz2}$ mice were surgically joined in parabiosis as previously described (Kamran et al., 2013). After lateral skin incisions were performed from the elbow toward knee in each mouse, olecranon and knee joints were tied together using non-absorbable 3-0 suture and the skin incisions were connected with a continuous absorbable 5-0 Vicryl suture. Mice were housed in a clean cage with monolithic bedding and were given Enrofloxacin (0.25 mg/ml) in drinking water for prophylaxis of infection. Four weeks after parabiosis surgery, both mice were inoculated intranasally with IAV. At 15 days following infection, chimerism in the blood and lung were assessed by flow cytometry. Chimerism of each cell population was defined as %CD45.1$^+$/(%CD45.1$^+$ + %CD45.2$^+$) in CD45.2$^+$ mice, and as %CD45.2$^+$/(%CD45.1$^+$ + %CD45.2$^+$) in CD45.1$^+$ mice (Yao et al., 2018).

Cell depletion

For the depletion of AMs at the time of recovery, we injected 300 ng/mouse diphtheria toxin (DTX) into IAV infected WT, *Ctnnb1*$^{fl/fl}$, *Ctnnb1*$^{\Delta Lyz2}$, CD169-DTR ($_{DTR/+}$), CD169-DTR ($_{DTR/+}$)/*Ctnnb1*$^{fl/fl}$, and CD169-DTR ($_{DTR/+}$)/*Ctnnb1*$^{\Delta Lyz2}$ mice at day 8, 9 and 12 post infection.

Immunofluorescence staining

Mouse lungs were perfused and inflated with 20 ml/kg aqueous buffered zinc formalin (Z-FIX; Anatech, Battle Creek, MI) immediately following euthanasia and used for paraffin-embedding. Immunofluorescence staining was performed as described previously (Lee et al., 2017). Paraffin-embedded tissue sections (5 μm) were rehydrated and subjected to antigen retrieval in Tris-HCl buffer (100 mM, pH 9.5). Blocking was performed with 15% BSA in 0.2% Triton-X/PBS at room temperature for 60 min. Sections were incubated with chicken anti-GFP (1:500, Abcam, ab13970) and goat anti-SP-C (1:50, Santa Cruz Biotechnology, sc-7706) overnight at 4°C. The immune complexes were detected using Alexa Fluor 568 donkey anti-goat or Alexa Fluor 488 goat anti-chicken (1:400, Invitrogen) secondary antibodies before sections were counterstained with DAPI. Sections were mounted in Prolong Gold antifade reagent (Invitrogen). Fluorescence images were acquired using a Zeiss microscope.

Tamoxifen treatment

To induce gene recombination in *Ctnnb1*$^{fl/fl}$ or *Ctnnb1*$^{\Delta Spc\text{-}cre\ ERT2}$ mice, tamoxifen (Sigma-Aldrich) was dissolved in warm sunflower oil (Sigma-Aldrich) and administered via daily intraperitoneal injection for five consecutive times. Each application was 2 mg/mouse at a concentration of 20 mg/ml.

Lung histopathology

Mice were perfused with PBS (10 mL) via the right ventricle following euthanasia. Paraformaldehyde (PF, 10%) was then gently instilled into the lung and left inflated for one minute before excising and moving lobe to 10% PF for 48 hours followed by transfer to ethanol (70%). Samples were shipped to Mayo Clinic Histology Core Lab (Scottsdale, AZ) where they were embedded in paraffin and 5 μm sections were cut for Hematoxylin and eosin stain. To quantify percent of inflamed or disrupted alveolar area, slides were scanned through the Aperio whole slide scanning system (Leica) and exported to image files. Computer-based image analysis was performed using the ImageJ software (NIH, Bethesda, MD, USA). We first determined the total lung area by converting the image into gray scale, followed by red highlighting through the adjustment of the threshold. For determination of the inflamed and disrupted area, color images were split into single channels. We then used the green channel, highlighted the inflamed areas in red by adjusting the threshold and measured the areas based on pixel. The percentages of disrupted and inflamed lung areas were calculated based on the ratio of highlighted disrupted areas to the total lung area in each lung section.

Co-immunoprecipitation

AMs were obtained from the BAL of 15 naive WT C57BL6 mice and pooled for culturing *in vitro*. AMs or B16 cell lines were treated with or without 100 ng/ml of Wnt3a in complete RPMI-1640 medium for overnight. For AMs, 10 ng/ml GM-CSF was added. Then, the treated cells were collected in RIPA buffer and lysed for 1h on ice. After being centrifuged for 10 min at 12,000 rpm, 10% of the soluble lysate was set aside as input, and the remainder was incubated with indicated antibody at 4°C overnight on a rotating shaker and then

incubated with Protein A/G Plus-agarose (Santa Cruz, sc-2003) at 4°C for 2 h. The immunoprecipitates were mixed with loading buffer and boiled for 10 min at 95°C. The precipitated proteins were subjected to western blot analysis.

Western blot analysis

Cultured or FACS-sorted cells were lysed in lysis buffer (62.5mM Tris-HCL (pH 6.8), 2% SDS and 10% glycerol) with a protease inhibitor cocktail (Roche). The lysates were separated by SDS-PAGE and immunoblotted using antibodies against active β-catenin (1:1000, Cell Signaling Technology), total β-catenin (1:1000, Cell Signaling Technology), HIF-1α (1:1000, Cell Signaling Technology) or β-actin (1:5000, Santa Cruz Biotechnology).

Metabolic analysis

Real-time oxygen consumption rate (OCR) and extracellular acidification rate (ECAR) of AMs were measured using a Seahorse XFp Analyzers (Seahorse Bioscience) (Li et al., 2019). 1×10^5 AM were seeded into each well of Seahorse XFp Cell Culture Miniplates, and pre-treated with or without 100 ng/ml Wnt3a for overnight at 37°C and 5% CO_2. On the following day, the cells were washed twice and incubated at 37°C for 1 h in the absence of CO_2 in unbuffered assay medium (pH = 7.4, Agilent Technologies) with 10 mM glucose for mitochondrial stress test or without glucose for glycolytic stress test. OCR and ECAR were measured under basal conditions and after the addition of the following compounds: 1 μM oligomycin, 1.5 μM FCCP (carbonyl cyanide-4-(trifluoromethoxy) phenylhydrazone), 0.5 μM rotenone + 0.5 μM antimycin, 10 mM glucose, and 50 mM 2-DG (2-deoxy-D-glucose) (all compounds obtained from Sigma) as indicated in the text. Data were analyzed with Wave Desktop software version 2.6 (Agilent Technologies).

Transmission electron microscopy

In vitro cultured AMs or sorted AMs were fixed in 2% paraformaldehyde and 2.5% glutaraldehyde in 0.1 M sodium cacodylate. Following fixation, cells were embedded and sliced for transmission electron microscopy. The Grids were imaged with a JEM 1400 transmission electron microscope (JEOL). Mitochondrial morphology was scored as normal or abnormal. Structurally abnormal mitochondria were defined operationally as those with loss of cristae, decreased electron density of the matrix, loss of integrity of mitochondrial membrane and/or the formation of autophagosomes structures as reported before (Sohn et al., 2013). The number of damaged mitochondria per cell was quantified.

Bone marrow chimera

For generation of bone marrow chimeric mice, WT recipient mice were lethally irradiated (1100 Rads) and then i.v. injected ~4 million bone marrow cells from *Ctnnb1*$^{fl/fl}$, *Ctnnb1*$^{\Delta Lyz2}$ or *Egln3*-YFP mice. Experimental chimeric mice were infected with IAV at 10 weeks post reconstitution.

Single-cell RNA sequencing

Wnt3a-treated AMs or control AMs were loaded on the Chromium Controller (10x Genomics). Single-cell libraries were prepared using the Chromium Single Cell 3′ Reagent kit (10x Genomics) following manufacturer's instruction. Paired-end sequencing was performed using an Illumina HiSeq 2500 in rapid-run mode. CellRanger software package (10x Genomics) were used to align and quantify sequencing data from 10x Genomics. All scRNA-seq analyses were performed in R (version 3.4.0) using the package Seurat (version 3.0) (Stuart et al., 2019). To analyze the cell cycle signature from the dataset, we used Seurat to calculate a cell cycle score for each cell based on expression across a list of reported core gene set including 43 G1/S and 54 G2/M markers (Macosko et al., 2015; Tirosh et al., 2016). Scaled residual expression obtained from Seurat modeling the relationship between gene expression and the cell cycle scores, that was used for dimensionality reduction and clustering. UMAP dimensional reduction was performed to visualize data in 2D space. DEGs between clusters were determined using a Wilcoxon rank sum test. For functional analysis, GSEA (Subramanian et al., 2005) was applied to identify gene sets that have statistically significant differences between control and Wnt3a treated AMs.

RNA-seq

Total RNA from *in vitro* cultured AMs was extracted using RNeasy Plus Mini Kit (QIAGEN) following the manufacture's protocol. Two pools per genotype were used for RNA-seq. After quality control, high quality (Agilent Bioanalyzer RIN > 7.0) total RNA was used to generate the RNA sequencing library. cDNA synthesis, end-repair, A-base addition, and ligation of the Illumina indexed adapters were performed according to the TruSeq RNA Sample Prep Kit v2 (Illumina, San Diego, CA). The concentration and size distribution of the completed libraries was determined using an Agilent Bioanalyzer DNA 1000 chip (Santa Clara, CA) and Qubit fluorometry (Invitrogen, Carlsbad, CA). Paired-end libraries were sequenced on an Illumina HiSeq 4000 following Illumina's standard protocol using the Illumina cBot and HiSeq 3000/4000 PE Cluster Kit. Base-calling was performed using Illumina's RTA software (version 2.5.2). Paired-end RNA-seq reads were aligned to the mouse reference genome (GRCm38/mm10) using Bowtie (v2.3.4). Pre- and post-alignment quality controls, gene level raw read count and normalized read count (i.e., FPKM) were performed using RSeQC package (v2.3.6) with NCBI mouse RefSeq gene model. Differential expression for each gene between various groups specified in the text was identified by Cuffdiff (Trapnell et al., 2010).

Chromatin immunoprecipitation (ChIP)

AMs were obtained from the BAL of naive WT C57BL6 mice (30 mice per experiment), culturing *in vitro* in the presence of 100 ng/ml Wnt3a, and were subjected to ChIP assay as previously described (Yao et al., 2013). In brief, $8x10^6$ AM were crosslinked for 10 min at 37°C by the addition of 1% freshly made formaldehyde. Fixed cells were pelleted at 4°C and washed with ice-cold PBS. The cells were lysed with SDS lysis buffer (1% SDS, 10mM EDTA, 50mM Tris, pH 8.1) containing protease inhibitors (Roche) on ice for 10 min and sonicated to an average size of 200-500bp. After sonication, samples were centrifuged at 13,000 rpm for 10 min at 4°C and 5% of sonicated cell extracts were saved as input. The resulting whole-cell extract was incubated with Protein A/G Agarose (Santa Cruz) for 1h at 4°C. Precleared extracts were then incubated with 60 ul of Protein A/G Agarose (Santa Cruz) for ChIP with 5 μg of the appropriate antibody overnight at 4°C. ChIP antibodies against β-catenin or HIF-1α and control antibodies were from Cell Signaling Technology. After overnight incubation, beads were washed once with low salt immune complex wash buffer (0.1% SDS, 1% Triton X-100, 2 mM EDTA, 20 mM Tris-HCL pH 8.1, 150 mM NaCl), once with high salt immune complex wash buffer (0.1% SDS, 1% Triton X-100, 2 mM EDTA, 20 mM Tris-HCL pH 8.1, 500 mM NaCl), once with LiCl wash buffer (10 mM Tris-HCl pH 8.1, 1 mM EDTA, 250 mM LiCl, 1% NP-40), and twice with TE wash buffer (10 mM Tris-HCl pH 8.0, 1 mM EDTA). DNA was eluted in freshly prepared elution buffer (1% SDS, 0.1M NaHCO3). Cross-links were reversed by overnight incubation with 5 M NaCl at 65°C. RNA and protein were digested using RNase A and proteinase K (Roche), respectively, and DNA was purified by QIAGEN MinElute PCR Purification kit according to the manufacturer's instructions. The immunoprecipitated DNA was analyzed by quantitative real-time PCR and normalized relative to input DNA amount. Primers were designed to a segment that was centered on the β-catenin and HIF-1α coverage regions. Primers used in this study are listed in Table S1. Real-time PCR data is represented as fold levels over control.

BrdU incorporation

For BrdU incorporation *in vivo*, indicated mice were infected with IAV. At day 7 p.i., BrdU (Sigma, 1 mg/ mouse in PBS) was injected through i. p. At day 8 p.i., mice were sacrificed, and lung cells were collected as described (Sun et al., 2009). Cells were surface stained with Siglec F, CD11c, CD11b and Ly6G, and intracellular BrdU staining was performed using the BrdU flow kit (BD Bioscience) as described in manufacturer's manual. For BrdU in corporation *in vitro*, AM were pre-treated with or without Wnt3a (100 ng/ml) in complete RPMI-1640 medium without GM-CSF for overnight. Subsequently, cells were washed with warm PBS and treated with or without Wnt3a (100 ng/ml) in complete medium with 10 ng/ml GM-CSF for another overnight. AMs were pulsed with 10 μM BrdU at 12 h before experimental end-point. BrdU incorporation in AMs was measured.

Cell cycle analysis

For cell cycle analysis *in vitro*, 2×10^5 AM were pre-treated with or without Wnt3a (100 ng/ml) in complete RPMI-1640 medium for overnight. Subsequently, cells were washed with warm PBS and treated with or without Wnt3a (100 ng/ml) in complete medium in the presence of 10 ng/ml GM-CSF for another overnight. Then, the cells were fixed with 70% ethanol at 4°C for at least 2h. For DNA labeling with propidium iodide (PI), the fixed cells were washed twice with PBS and the pellet was incubated with 200 μL of solution containing 50 μg/ml PI plus 550 U/ml RNase in PBS for 30min at 37°C according to manufacturer's instructions (abcam, ab139418). The samples were analyzed on flow cytometer.

Lung and bone marrow cell suspension preparation

Lungs were cut into small pieces, and digested with Collagenase Type 2 (Worthington Biochemical) for 30 min at 37°C. Cells were further passed through 70 μm cell strainer (Falcon) and washed with flow cytometry buffer. After red blood cell lysis, cells were centrifuged and re-suspended in cold flow cytometry buffer for flow cytometry analysis. The bone marrow cells were collected from tibias and femurs by flushing with cold PBS through a 25 gauge needle. The single cell suspension was passed through a 70 μm cell strainer in a 50 mL falcon tube. Cells were pelleted at 1,600 rpm for 5 min, and the pellet was suspended in ACK lysis buffer (0.15 M NH_4Cl, 1 mM $KHCO_3$, 0.1 mM Na_2EDTA, pH 7.2) at room temperature for 5 min. After centrifugation at 1,600 rpm for 5 min, the cell pellet was suspended in cold PBS.

Flow cytometry analysis

Fluorescence-conjugated FACS Abs were purchased from Biolegend, BD Biosciences, eBioscience or Tonbo biosciences. Ab clones are provided. Cell staining was performed with the appropriate antibody cocktail in flow cytometry buffer. The cell populations were defined based on following cell surface markers: AM ($CD11c^+$ Siglec F^+ $CD11b^{low}$ $CD64^+$ $MerTK^+$), NAM ($CD169^+CX3CR1^+$ $CD11c^-$), Neutrophils ($CD11b^+$ $Ly6G^+$), total $CD11b^+$ Monocyte/Macrophage population ($Ly6G^-$ Siglec F^- $CD11b^+$), Inflammaotry Monocytes ($Ly6G^-$ Siglec F^- $CD11b^+$ $Ly6c^+$), $CD11b^+$ Macrophages ($Ly6G^-$ Siglec F^- $CD11b^+$ $CD64^+$), NP_{366} tetramer$^+$ cells ($CD8^+$ NP_{366}-tet^+), PA_{224} tetramer$^+$ cells ($CD8^+$ PA_{224}-tet^+). Samples were collected on FACS Attune or FACS Attune NXT flow cytometer (Life technologies) and analyzed using Flow Jo software (Tree Star).

For intracellular staining, cell suspensions were stained for surface marker at 4°C for 30 min. Cells were washed twice with FACS buffer (PBS, 2 mM EDTA, 2% FBS, 0.09% Sodium Azide), prior to fixation and permeabilization with the Foxp3 transcription factor staining buffer set (eBioscience) for 1 h at RT in the dark. Cells were washed twice with perm wash buffer (eBioscience), and stained

with Abs against active β-catenin (Cell Signaling Technology), HIF-1α (Cell Signaling Technology), Ki67 (eBioscience) and control immunoglobulin (Biolegend) for at least 30 min at RT, and washed twice with perm wash. Samples were processed with flow cytometer.

Apoptosis analysis

AM apoptosis was assessed by Annexin V and 7-AAD staining using an apoptosis detection kit (APC Annexin V Apoptosis Detection kit, Biolegend) according to the manufacturer's instructions. For detection of active caspase-1 activities in AMs, cells were incubated with active caspase-1 detection reagent (FLICA 660 Caspase-1 Assay, Immunochemistry Technologies) for 45 min at 37 C as described in the manufacturer's instructions.

HIF-1α inhibitor treatment

HIF-1α inhibitor LW6 was purchased from TargetMol (Catalog No. T3494), and was dissolved in DMSO. WT mice were intranasally infected with IAV, and DMSO or LW6 (30 mg/kg) was administered intraperitoneally daily from 1 d post-infection for 3 days or 8 days. Mice were monitored for body weight change and the BAL and lungs were harvested for analysis at day 4 or day 14 p.i.

QUANTIFICATION AND STATISTICAL ANALYSIS

Data are mean ± SEM of values from individual mice (*in vivo* experiments). Unpaired two-tailed Student's t test (two group comparison), one-way ANOVA (multiple group comparison), Multiple t tests (weight loss and Multiplex studies) or Logrank test (survival study) were used to determine statistical significance by GraphPad Prism software. We consider *P value*s < 0.05 as significant. *, $p < 0.05$; **, $p < 0.01$; ***, $p < 0.001$.